Effect of Powder Shape and Size on the Properties of Low-Viscosity Iron-Based Feedstock Used in Low-Pressure Powder Injection Molding

by

Seyed Mohammad MAJDI

THESIS PRESENTED TO ÉCOLE DE TECHNOLOGIE SUPÉRIEURE
IN PARTIAL FULFILLMENT FOR A MASTER'S DEGREE
WITH THESIS IN MECHANICAL ENGINEERING
M.A.Sc.

MONTREAL, JUNE 13, 2021

ÉCOLE DE TECHNOLOGIE SUPÉRIEURE
UNIVERSITÉ DU QUÉBEC

Seyed Mohammad Majdi, 2021

.

This Creative Commons license allows readers to download this work and share it with others as long as the author is credited. The content of this work cannot be modified in any way or used commercially.

BOARD OF EXAMINERS

THIS THESIS HAS BEEN EVALUATED

BY THE FOLLOWING BOARD OF EXAMINERS

Mr.Vincent Demers, Thesis Supervisor
Department of Mechanical Engineering, École de technologie supérieure

Mr. Vladimir Brailovski, Thesis Co-supervisor
Department of Mechanical Engineering, École de technologie supérieure

Mr. Jean-François Chatelain, Board of Examiners
Department of Mechanical Engineering, École de technologie supérieure

Mr. Lucas Hof, Member of the jury
Department of Mechanical Engineering, École de technologie supérieure

THIS THESIS WAS PRESENTED AND DEFENDED

IN THE PRESENCE OF A BOARD OF EXAMINERS AND PUBLIC

AUGUST 2, 2021

AT ÉCOLE DE TECHNOLOGIE SUPÉRIEURE

ACKNOWLEDGMENT

I would like to express my gratitude to Prof. Vincent Demers, my thesis supervisor, for his excellent availability and interest in this research work. I also would like to thank Prof. Vladimir Brailovski, my thesis co-director of memory, who has immensely supported me in my research.

Many thanks also to all members of the jury for agreeing to judge this work. Finally, I owe my deepest gratitude to my colleague, Atefeh, for her contributions and for sharing her knowledge, as well as my parents and sister for their unconditional support, love, and patience.

EFFET DE LA FORME ET DE LA TAILLE DE LA POUDRE SUR LES PROPRIÉTÉS DES MÉLANGES FAIBLE VISCOSITÉ À BASE DE FER UTILISÉS DANS LE MOULAGE PAR INJECTION DES POUDRES À BASSE PRESSION

Seyed Mohammad MAJDI

RÉSUMÉ

Le moulage par injection de poudre basse pression (LPIM) est une technologie avancée de fabrication rentable pour produire des volumes de production faibles ou élevés de pièces métalliques de forme complexe avec de bonnes propriétés mécaniques. Bien qu'il y ait eu quelques études menées sur les poudres métalliques de forme sphérique, il y a une mauvaise compréhension de l'application des poudres métalliques de forme irrégulière sur les propriétés mécaniques et la densité des composants frittés produits par LPIM. Les travaux de recherche de ce projet présentent donc une approche expérimentale pour étudier l'effet de la forme et de la taille de la poudre sur les propriétés des pièces métalliques fabriquées par LPIM. Quatre mélanges poudre-liant de faible viscosité ont été préparés en utilisant trois poudres de fer de forme irrégulière, tamisées suivant trois tailles de maille et étiquetées comme -10, -20, -45 µm, et une poudre de fer carbonyle sphérique (CIP) avec une taille moyenne de 4 µm. Le système de liant était composé de 1 vol. % d'acide stéarique, 2 vol. % de cire de carnauba, 2 vol. % d'éthylène-acétate de vinyle pour leurs effets tensioactifs, démoulants et épaississants, respectivement, et le reste du liant était composé de cire de paraffine. Des échantillons rectangulaires ont été injectés à débit volumétrique constant et déliantés thermiquement dans un média mèche et frittés à haute température sous hydrogène. Les profils de viscosité des mélanges ont été obtenus en utilisant un rhéomètre rotatif. La densité de la poudre, des liants polymériques et des mélanges ont été mesurés en utilisant un pycnomètre à gaz. En outre, pour obtenir le point de fusion des matières premières et la température de dégradation du liant, un test de calorimétrie différentielle à balayage (DSC) et une analyse thermogravimétrique (TGA) ont été effectués, respectivement. La densité des échantillons frittés a été mesurée en utilisant la méthode d'imprégnation à l'huile basée sur le principe d'Archimède. Enfin, la structure du réseau délianté et les observations métallographiques des pièces frittées ont été réalisées à l'aide d'un microscope électronique à balayage (SEM) et d'un microscope optique, respectivement. Il a été montré qu'une poudre irrégulière à base de fer de -45 µm peut être mélangée avec une fraction volumique supérieure à la poudre -10 µm, ce qui entraîne une légère augmentation de la densité relative qui est corrélée avec l'analyse métallographique montrant un niveau plus élevé de pores isolés de la pièce frittée.

Mots clés: moulage par injection de poudre basse pression (LPIM); poudre de fer; particules irrégulières; liants; déliantage; température de pré-frittage; frittage

EFFECT OF POWDER SHAPE AND SIZE ON THE PROPERTIES OF LOW-VISCOSITY IRON-BASED FEEDSTOCK USED IN LOW-PRESSURE POWDER INJECTION MOLDING

Seyed Mohammad MAJDI

ABSTRACT

Low-pressure powder injection molding (LPIM) is a cost-effective advanced manufacturing technology to produce low or high production volumes of complex-shaped metal parts with good mechanical properties. Although there has been some study conducted on spherical-shaped metal powders, there is a poor understanding of the application of irregularly-shaped metal powders on the physical and micro-structural such as density of the sintered components produced by LPIM. The current research work presents an experimental approach to investigate the effect of powder shape and size on the properties of metallic parts fabricated by LPIM. Four low-viscosity feedstocks were prepared using three irregularly-shaped iron powders, sieved in three mesh sizes, and labeled as -10, -20, -45 µm, and one spherical carbonyl iron powder (CIP) with an average particle size of 4 µm. The binder system consisted of 1 vol. % of stearic acid, 2 vol. % of carnauba wax, 2 vol. % of ethylene-vinyl acetate for their surfactant, demolding, and thickening effects, respectively, and where the balance of the binder was constituted of paraffin wax. Rectangular specimens were injected at constant volumetric flow and thermally wick-debound and sintered at high temperatures under a hydrogen atmosphere. The feedstock viscosity profiles were obtained using a rotational rheometer. The density of powder, polymeric binders, and feedstock were measured using a gas pycnometer. The melting point of the feedstocks and the binders' burnout temperatures were obtained using differential scanning calorimetry tests (DSC) and thermogravimetric analysis (TGA), respectively. The density of sintered specimens was measured using the oil-impregnation method based on Archimedes' principle. Finally, the debinding network and metallographic observations of the sintered parts were performed using a scanning electron microscope (SEM) and optical microscope, respectively. It has been shown that the -45 µm mesh irregular iron-based powder can be blended at higher solid loading as compared to -10 µm powder resulting in a slight increase in the relative density that was correlated with metallographic analysis showing a higher level of isolated pores in sintered part.

Keywords: low-pressure powder injection molding (LPIM); iron powder; irregular particles; binders; debinding; pre-sintering temperature; sintering

TABLE OF CONTENTS

Page

INTRODUCTION 1

CHAPTER 1 LITERATURE REVIEW 3
1.1 Powder injection molding..3
1.2 Comparison between LPIM & HPIM processes..5
1.3 Feedstocks preparation..6
  1.3.1 Metallic powders..7
  1.3.2 Binders 9
1.4 Injection molding 10
1.5 Debinding..13
1.6 Sintering...18
1.7 Properties of sintered component...19

CHAPTER 2 PROBLEM DEFINITION AND RESEARCH OBJECTIVES 23
2.1 Problem definition 23
2.2 Research objectives...23

CHAPTER 3 EXPERIMENTAL METHODOLOGY 25
3.1 Feedstock formulations...25
3.2 Feedstocks characterization 27
  3.2.1 Measuring density and critical solid loading 27
  3.2.2 Measuring the melting point and decomposition of binders and feedstocks 28
  3.2.3 Measuring viscosity 30
3.3 Injection process 30
3.4 Debinding and sintering cycles...31
3.5 Characterization of the debound and sintered properties.........................32

CHAPTER 4 EFFECT OF POWDER SHAPE AND SIZE ON THE PROPERTIES OF LOW VISCOSITY IRON-BASED FEEDSTOCK USED IN LOW-PRESSURE POWDER INJECTION MOLDING....................................37
4.1 Abstract..37
4.2 Introduction...38
4.3 Experimental procedure..40
  4.3.1 Materials and feedstock characterization...40
  4.3.2 Injection, debinding, and sintering...44
4.4 Results and discussion 47
  4.4.1 Evaluation of the maximum solid loading, melting point, and viscosity of feedstocks 47
  4.4.2 Design of the debinding cycle and characterization of the debound parts 50

4.4.3 Sintered properties 53
4.5 Conclusion 54
4.6 Acknowledgments..55

CONCLUSIONS..57

RECOMMENDATIONS..59

REFERENCES 61

LIST OF TABLES

Page

Table 1-1 Comparison between injection machines used in HPIM and LPIM 11

Table 1-2 Research studies on the influence of metal powder characterizations on properties of sintered components..22

Table 3-1 Standard protocol for polishing sintered samples 35

Table 4-1 Characteristics of iron powders...43

Table 4-2 Characteristics of binder constituents...44

Table 4-3 Characteristics of the feedstocks 50

LIST OF FIGURES

Page

Figure 1-1 An overview of the powder injection molding process taken from Dehghan-Manshadi, Yu, Dargusch, StJohn, & Qian (2020, p. 191) 3

Figure 1-2 Example of components produced using MIM taken from Wikimedia Foundation (2021) 4

Figure 1-3 Comparison between the LPIM and HPIM processes taken from Vincent Demers (2019, p. 54) 6

Figure 1-4 Morphology of metal powders fabricated using (a) gas atomization stainless steel powder, (b) water atomization stainless steel powder, (c) chemically-reduced tungsten powder taken from R. M. German (2012, p. 59); Kong, Barriere, & Gelin (2012, p. 2174) 8

Figure 1-5 Influence of particle shape on packing density of mono-sized particles taken from R. M. German (2012, p. 54) 9

Figure 1-6 General view of the (a) HPIM taken from Donald F Heaney (2012, p. 119), and (b) LPIM injection molding machines taken from Lamarre et al. (2017, p. 2597) 12

Figure 1-7 Schematic of binder distributions in two-stage debinding presenting the condition of binders (a) during solvent debinding stage, (b) at the beginning of the thermal debinding stage, (c) halfway through thermal debinding, and (d) example of two particles partially bonded (also known as the pre-sintered condition) after the debinding stage taken from Hwang, Lin, & Lee (1997, p. 604); Vervoort et al. (1996, p. 136) 14

Figure 1-8 A schematic representation of the binder distribution during thermal wick-debinding taken from Gorjan, Dakskobler, & kosmač (2010, p. 3016) 15

Figure 1-9 Low-pressure injection molded sample debound: (a) without wicking embedment using high-temperature debinding, and (b) with wicking embedded in highly porous alumina using low-temperature debinding taken from Gorjan (2012, p. 99) 16

Figure 1-10 Thermal properties of wax-based feedstock obtained by (a) DSC, (b) TGA taken from Vincent Demers (2019, p. 60) and (c) typical thermal debinding and pre-sintering cycle for iron powder taken from Santos, Neivock, Maliska, Klein, & Muzart (2005, p. 510) 17

Figure 1-11 Evolution of the microstructure in sintering step in PIM involving the initial bonding of the particles followed by pore rounding and grain bounding and consequently final stage taken from Randall M German & Bose (1997, p. 226) 18

Figure 1-12 State of components prepared from bronze metallic feedstock taken from Contreras et al. (2009, p. 5620) 19

Figure 1-13 Microstructure of sintered components produced from irregularly-shaped stainless particles of different sizes: (a) -100 mesh powder, (b) -200 mesh powder; and (c) -400 mesh powder taken from Hu et al. (2018) 20

Figure 1-14 (a) Relative density (b) tensile strength of water-atomized stainless steel powders sintered at different temperatures taken from Hu et al. (2018) 20

Figure 1-15 Influence of particle shape on the relative density of bronze sintered parts at different sintering temperatures taken from Contreras et al. (2009, p. 5623) 21

Figure 3-1 The four step required to produce a MIM part 25

Figure 3-2 The appearance of the binders at room temperature a) paraffin wax, b) carnauba wax, c) stearic acid, and d) ethylene-vinyl acetate 26

Figure 3-3 a) Feedstock mixture and b) vacuum container 27

Figure 3-4 Pycnometer machine 28

Figure 3-5 DSC equipment 29

Figure 3-6 TGA equipment 29

Figure 3-7 a) Rheometer equipped with a Peltier temperature-controlled system b) cross-section of the concentric-cylinder cell 30

Figure 3-8 a) Exploded view of the rectangular mold, b) rectangular steel mold, and c) low-pressure injection machine 31

Figure 3-9 Overview of a) debinding and b) sintering furnaces setup 32

Figure 3-10 Scanning electron microscope 33

Figure 3-11 Archimedes' density measurement setup 34

Figure 3-12 (a) Olympus GX51 inverted metallurgical microscope (b) mounted sample, (c) Struers Labopress semi-automatic machine, and (d) Buehler Motopol 2000 automatic polishing machine 35

Figure 4-1 SEM micrographs and particle size distributions of four iron-based powder lots: (a, e) -45 µm, (b, f) -20 µm, (c, g) -10 µm, and (d, h) CIP 42

Figure 4-2 (a) Schematic view of the LPIM injection press, and (b) exploded view of the rectangular mold used during injections 45

Figure 4-3 Debinding setup illustrating the (a) injected parts settled on a compacted alumina bed in a boat, (b) parts buried in the powder bed, (c) sintering cycle, and (d) overall dimensions of the i-injected, ii-debound, iii-sintered.................................46

Figure 4-4 Determination of the critical and maximum solid loadings of the feedstocks prepared with (a) -45 µm, (b) -20 µm, (c) -10 µm, and (d) CIP powders 48

Figure 4-5 (a) DSC results obtained during heating (2nd cycle), (b) viscosity profile obtained at 80°C for feedstocks prepared with -45 µm, -20 µm, -10 µm, and CIP powders 49

Figure 4-6 (a) TGA profiles obtained with feedstocks, (b) thermal wick-debinding profile designed based on the DSC and TGA results...51

Figure 4-7 SEM micrographs of the cross-section (a-d) at the center (left column) and (e-h) edge (right column) of the brown specimens produced from -45 µm, -20 µm, -10 µm, and with CIP powders 52

Figure 4-8 (a) Sintered density and optical micrographs of (b) -45 µm, (c) -20 µm, (d) -10 µm, (e) CIP as-polished specimens after sintering (bright phase: iron, and black phase: pores)..54

LIST OF ABBREVIATIONS

PIM	Powder Injection Molding
MIM	Metal Injection Molding
CIM	Ceramic Injection Molding
LPIM	Low-Pressure Powder Injection Molding
HPIM	High-Pressure Powder Injection Molding
MPIM	Micro-Pressure Powder Injection Molding
PW	Paraffin Wax
CW	Carnauba Wax
SA	Stearic Acid
EVA	Ethylene-vinyl Acetate
DSC	Differential Scanning Calorimetry
TGA	Thermogravimetric Analysis
SEM	Scanning Electron Microscope

LIST OF SYMBOLS

T	Temperature (°C)
P	Pressure (MPa)
ρ	Density of particles (g/cm^3)
t	Time (h)
$\mathrm{T_m}$	Melting point temperature (°C)
$\mathrm{T_D}$	Degradation temperature (°C)

INTRODUCTION

This thesis summarizes a Master's project with collaboration between École de technologie supérieure (ÉTS, Montreal, Qc, Canada) and Rio Tinto Metal Powders (RTMP, Sorel-Tracy, Qc, Canada). In general, the casting might be considered the only desirable production technique to produce complex shape metallic parts. However, because of the inferior mechanical qualities of components made with this technology, manufacturers have turned to metal injection molding (MIM) to create complex designs similar to casting but exhibiting better in-service performance. Low-pressure metal injection molding (LPIM) is a relatively recent process that allows for the creation of metallic parts with high density and mechanical qualities at a lower cost than traditional high-pressure metal injection molding (HPIM). In the LPIM, obtaining a low-viscosity feedstock and a high-moldability mixture allows for the manufacturing of more complex-shape components with low tonnage injection machines and small overall mold resulting in lowering production costs.

Generally, the LPIM process consists of mixing the metallic powder with molten polymeric binders to obtain a feedstock. This mixture is then injected into a mold cavity to produce simple- or complex-shaped parts. Subsequently, debinding and sintering heat treatments are performed to remove the binders entirely and obtain a near-net-shape dense metallic component, respectively. Since no study has been conducted on the evaluation of sintered properties of LPIM feedstocks, assessing the full potential of this manufacturing technology is still limited by a poor understanding of elements that could influence the properties of sintered parts. Therefore, this research project specifically aimed to focus on debinding and sintering steps of LPIM to understand and interpret better the effect of powder parameters (e.g., particle size distribution and shape) on the physical and micro-structural such as density of iron-based parts manufactured by this processing approach.

This research report is divided into four chapters. The first chapter is a literature review, in which an overview of the MIM process terminology and each stage are reviewed. The second chapter presents the problem definition and research objectives. The experimental methodologies used for this work are described in chapter 3. The fourth chapter presents a journal article that discusses the effect of shape and size of iron powder on the properties of low-viscosity iron-based feedstock used in low-pressure injection molding (published in journal of *Powder Metallurgy*). Finally, a summary of the conclusions and some research recommendations are presented for future research works.

CHAPTER 1

LITERATURE REVIEW

1.1 Powder injection molding

Powder injection molding (PIM), including metal injection molding (MIM) or ceramic injection molding (CIM), is a process for forming near-net-shape components and producing small and complex-shape parts. A typical MIM process involves four subsequent steps consisting of feedstock preparation by mixing a metallic powder with molten polymer binder constituents, injection molding into the desired geometry to produce a green part, debinding process, and finally, sintering. The debinding and sintering processes are performed to completely remove the binders and promote solid-state diffusion to obtain a dense component (Hausnerova, Mukund, & Sanetrnik, 2017; Herranz, 2019; Hidalgo, Jiménez-Morales, & Torralba, 2012). Using a wide range of materials, a relatively smooth finished surface, adequate dimensional tolerances, and outstanding mechanical properties are some of the noticeable advantages of the MIM process (Atre, Weaver, & German, 1998). Besides, interesting features such as threads, serrations, and waffle patterns can be produced using the MIM process (Donald F Heaney, 2012).

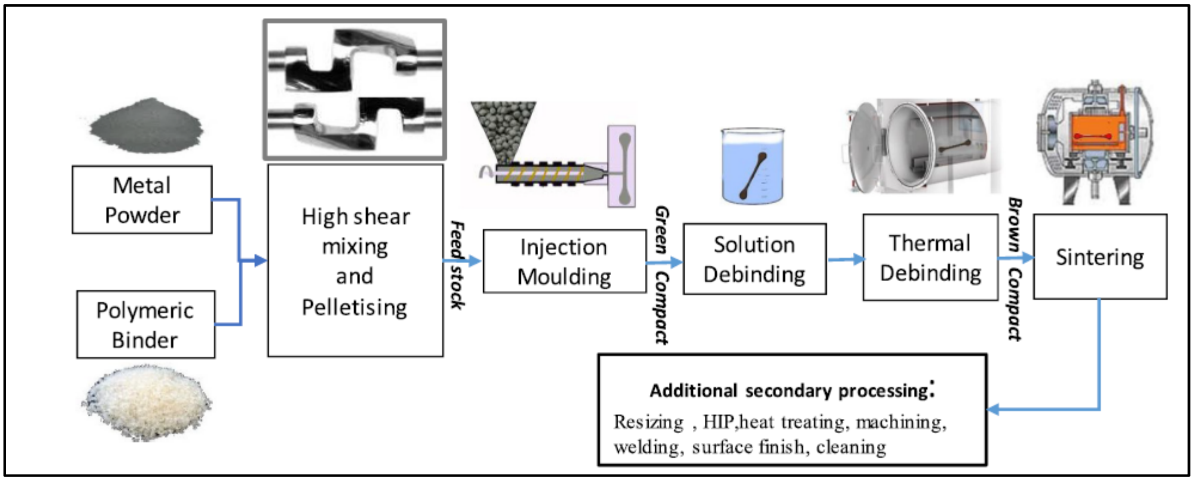
Metal Powder
Polymeric Binder
High shear mixing and Pelletising
Feed stock
Injection Moulding
Green Compact
Solution Debinding
Thermal Debinding
Brown Compact
Sintering
Additional secondary processing:
Resizing , HIP,heat treating, machining, welding, surface finish, cleaning

Figure 1-1 An overview of the powder injection molding process
taken from Dehghan-Manshadi, Yu, Dargusch, StJohn, & Qian (2020, p. 191)

As shown in Figure 1-2, various complex shape components are produced with application in the automotive industry. Many complex-shape components in medical, aerospace, military, jewelry, electronics, and many other industries are produced using the MIM process (Randall M German & Bose, 1997). The conventional MIM process is prominent in the large series production of parts with a similar rate and flexibility of plastic injection molding and geometric precision of powder metallurgy (this aspect is detailed below in section 2.2) (Hausnerova, 2011).

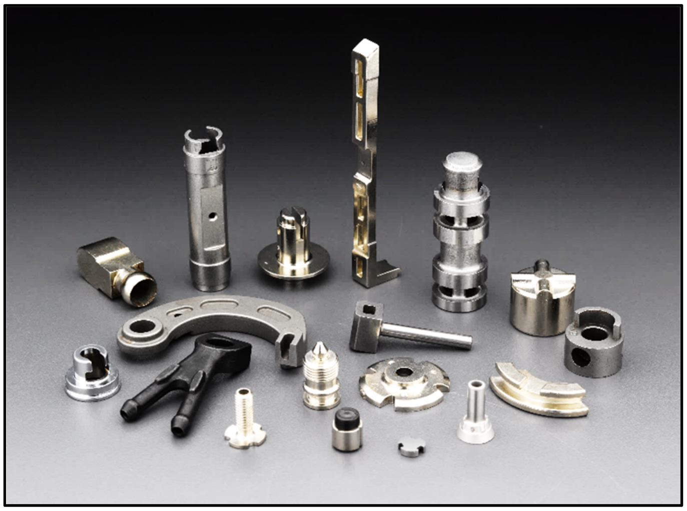

Figure 1-2 Example of components produced using MIM taken from Wikimedia Foundation (2021)

The first injection molding machine was built in the 1930s and used to produce ceramic-based feedstock compacts. Later in the 1970s and 1980s, demand for fabrication of components using ceramic powders with high mechanical properties in aerospace industries urges the further development of this technology (Mangels, 1994; Quevedo Nogueira, Bezerra, dos Santos, Sousa, & Acchar, 2001). Although new forming strategies, such as slip casting and hot isostatic pressing, have been successfully developed, the additional costs related to secondary operations still limit their progress (Medvedovski & Peltsman, 2012). Later, the developments made in plastic injection molding technology, using high pressure and high temperature to inject complex-shape polymeric components, were adapted to manufacture parts with superior mechanical properties from highly-filled polymeric suspensions containing ceramic or metallic particles. The current MIM market can be divided into several application fields where 20% of the applications constitute industrial components; 14%, automotive parts; 11%, electronic products; 9%, medical products, with the rest of the market occupied by military, aerospace, and jewelry applications, etc. (D.F. Heaney, 2019).

1.2 Comparison between LPIM & HPIM processes

As summarized in Figure 1-3, PIM is divided into two primary techniques: high-pressure powder injection molding (HPIM) and low-pressure powder injection molding (LPIM). As described by their names, the main difference between these two processes originated from the pressure required during the injection operation dictated by the binder system being used. In the HPIM, high-molecular-weight binders are used to produce a high-viscosity feedstock injected at high pressures and high mold clamping forces of about 500 MPa and 100 tons, respectively. In contrast, low-molecular-weight polymers and waxes are used in LPIM to produce a low-viscosity feedstock injected at a pressure less than 1 MPa with a mold clamping force of less than 1 ton. In HPIM, debinding is performed by different techniques, including a combination of thermal, solvent, and catalytic, while in LPIM, thermal wick-debinding is mainly used to remove the binders from the injected parts. In both HPIM and LPIM approaches, solid-state bonding of debound parts is achieved using similar well-known sintering techniques under different atmospheres such as vacuum, inert gas, or reactive gas.

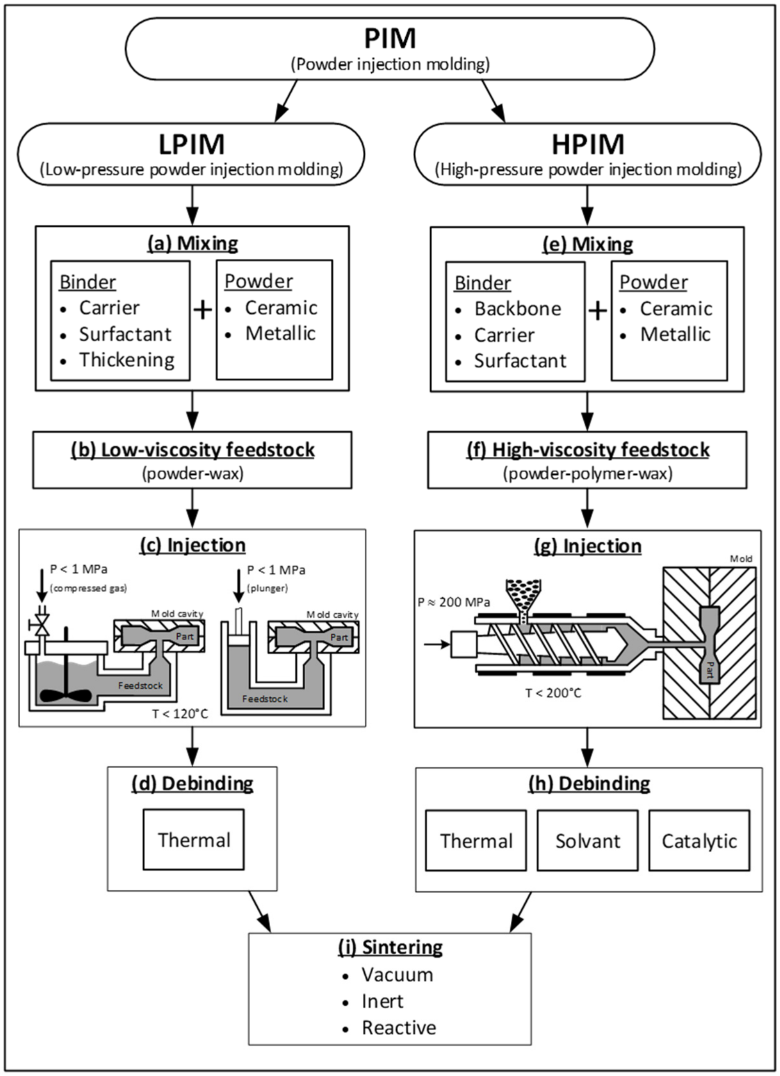
PIM
(Powder injection molding)
LPIM
(Low-pressure powder injection molding)
HPIM
(High-pressure powder injection molding)
(a) Mixing
Binder
• Carrier
• Surfactant
• Thickening
+
Powder
• Ceramic
• Metallic
(e) Mixing
Binder
• Backbone
• Carrier
• Surfactant
+
Powder
• Ceramic
• Metallic
(b) Low-viscosity feedstock
(powder-wax)
(f) High-viscosity feedstock
(powder-polymer-wax)
(c) Injection
P < 1 MPa
(compressed gas)
P < 1 MPa
(plunger)
Mold cavity
Part
Feedstock
Mold cavity
Part
Feedstock
T < 120°C
(g) Injection
Mold
P ≈ 200 MPa
Part
T < 200°C
(d) Debinding
Thermal
(h) Debinding
Thermal
Solvant
Catalytic
(i) Sintering
• Vacuum
• Inert
• Reactive

Figure 1-3 Comparison between the LPIM and HPIM processes taken from Vincent Demers (2019, p. 54)

1.3 Feedstocks preparation

The mixing process aims to coat the whole powder surface with polymer binders to obtain a homogenous powder-binder mixture known as a feedstock. Although the powders used in the HPIM and LPIM are similar, the significant differences rely on the binder types to produce low-viscosity (LPIM) or high-viscosity (HPIM) feedstocks. Specific details on metallic powders and binders used in PIM are presented below.

1.3.1 Metallic powders

As a key constituent in feedstock formulations, the metallic powder determines the design rules of the final MIM component to obtain the mechanical and dimensional properties required by the application. Generally speaking, powder characteristics, such as powder particle shape, average particle size, powder size distribution, and the tendency of powders to agglomerate, may significantly influence feedstocks' rheological properties. Zirconia, silicon nitride, stainless steel, iron, iron-nickel, cobalt-based superalloys, titanium, titanium alloys, and copper are the commercialized powders used in PIM. These powder lots are produced using different techniques, including gas atomization, water atomization, and electrochemical treatment that directly drive the particle characteristics such as the size, shape, microstructure, chemistry, and cost. Figure 1-4 presents typical powder morphologies produced with the above methods.

The spherical particles are produced generally using gas or plasma atomization and solid (carbonyl process) decomposition. This increase in particle sphericity improves the bulk density, reduces the feedstock viscosity, and produces high sinterability but increases the raw material cost. Although facilitating the feedstock flowability and injection process, the low interparticle friction associated with spherical powders may result in the slumps occurrence during debinding due to the extreme fragility of components (Contreras, Jiménez-Morales, & Torralba, 2009). In contrast, irregular particles mainly produced using the water atomization increase the strength of debound components, reduce the overall cost, but exhibit higher viscosity, lower packing density, and sinterability.

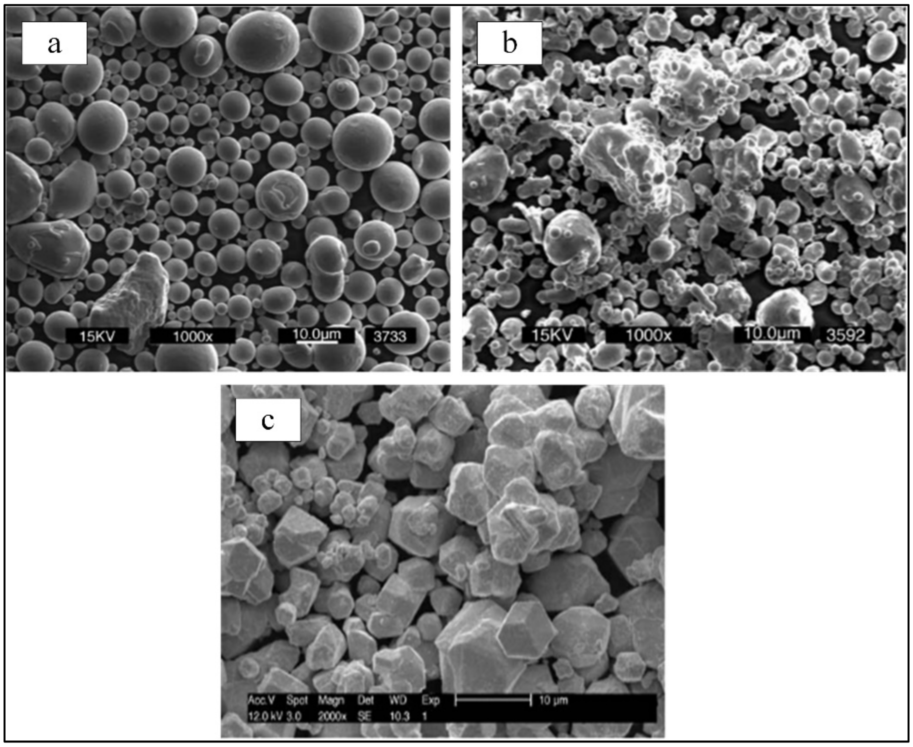

Figure 1-4 Morphology of metal powders fabricated using (a) gas atomization stainless steel powder, (b) water atomization stainless steel powder, (c) chemically-reduced tungsten powder taken from R. M. German (2012, p. 59); Kong, Barriere, & Gelin (2012, p. 2174)

Particle size distribution is one of the most used metrics to describe powder characteristics. Small particle sizes increase the viscosity of the feedstock, but also increase density after sintering due to their higher surface area.

The volume fraction of powder to binder (also known as the solid loading) is a critical parameter affecting the PIM feedstock viscosity. If the solid loading is too low, the feedstock has a low viscosity, which helps with injection but results in low particle contact, which may produce difficulties in maintaining the shape of the injected part during the debinding and sintering stages. On the other hand, a high solid loading can create large voids in the mixture and significantly increase viscosity, making injection difficult or impossible. To maximize the feedstock moldability and the powder sinterability, the feedstock should be formulated using an optimal solid loading, slightly lower than the critical value (typically 2 to 5% below the composition where the particles are packed together (Hidalgo et al., 2012). As a pioneer in

PIM, German (Randall M German & Bose, 1997) has suggested a solid loading ranging from 50 to 70 vol. % as a compromise between the injection and densification capabilities.

Scanning electron microscopy (SEM) commonly used to determine powder particle shape can also be applied to evaluate particle roundness. As illustrated in Figure 1-5, since higher packing density and lower viscosity could be achieved with spherical particles, they are preferable compared to irregular particles. Besides, as mono-sized powder lots exhibit lower packing densities, a wide powder size distribution is more favored for the PIM process (Atre et al., 1998; R. M. German, 2012).

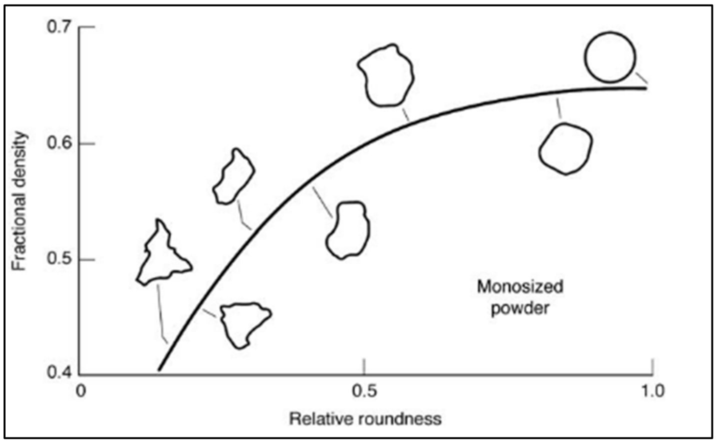

Figure 1-5 Influence of particle shape on packing density of mono-sized particles taken from R. M. German (2012, p. 54)

1.3.2 Binders

Generally speaking, a binder plays a critical role in the entire PIM process. The selection of binder constituents drives the feedstock flowability, prevents the powder/binder separation during and after the injection stage (inhomogeneous distribution of metal particles), acts as a transportation media for powders during injections, and maintains the shape of the injected part after solidification up to the debinding process (Randall M German & Bose, 1997; Schlechtriemen, Knitter, Haußelt, & Binder, 2013; Vervoort, Vetter, & Duszczyk, 1996). The key difference between the HPIM and LPIM binder systems lies in the absence of a backbone polymer (e.g., HDPE, PP, PS) in LPIM feedstocks. Such low-viscosity binders are generally constituted from waxes (a carrier), surfactants, and thickening agents, exhibiting similar solvent solubility and melting temperatures varying from 60 to 100°C. Binder systems in HPIM are formulated with backbone, carrier, and surfactant agents, exhibiting different solvent solubility and melting temperatures varying from 60 to 180°C. In the HPIM and LPIM feedstocks, the carrier is generally a wax-based binder made up of one or more natural or synthetic waxes, including paraffin wax, beeswax, microcrystalline wax, carnauba wax, montane wax, whale wax, wool wax, candelilla wax, ouricury wax, sugar cane wax, ozokerite wax, ceresin wax, or lignite wax (Adames, 2007; Kankawa, 1997). Surfactant agents, such as oleic acid, peanut oil, fish oil, or zinc stearate, are added to the carrier binder to enhance powder wettability, reduce feedstock viscosity, and improve feedstock homogeneity. In HPIM, the backbone constituent guarantees the sufficient strength of green parts and provides the shape retention of the compact after the primary binder removal through the solvent or catalytic debinding stages. These backbone polymers also referring to as secondary binders include low-density polyethylene (LDPE), polyethylene glycol (PEG), and high-density polyethylene (HDPE) (Hayat et al., 2017; Wongpanit, Khanthsri, Puengboonsri, & Manonukul, 2014; Ye et al., 2017). In LPIM, a thickening agent, such as ethylene-vinyl acetate (EVA), is added to the binder to increase viscosity and prevent powder and binder separation (Binet, Heaney, Spina, & Tricarico, 2005; Randall M. German, Hens, & Kin, 1991).

1.4 Injection molding

The second step of the PIM process is the injection, in which the molten feedstock is injected into a mold cavity, solidified, and ejected from the mold to produce the green part. The characteristics of the injection molding machines are summarized in Table 1-1, where the main differences reside in the temperature and pressure required to inject the feedstock into the mold.

Table 1-1 Comparison between injection machines used in HPIM and LPIM

Techniques	Feedstock temperature (°C)	Injection pressure (MPa)	Features
HPIM	150-200	150-200	• High-molecular-weight polymer • High-viscosity feedstock
LPIM	60-120	0.1-1	• Low-molecular-weight polymer • Low-viscosity feedstock

The injection stage illustrated in Figure 1-6a for the HPIM process starts by feeding raw materials (pelletized feedstock) through a hopper, which is then melted inside the cylinder by increasing the temperature up to the binder melting point. As the feedstock moves forward the rotating screw, the pressure, and temperature increase until the mixture reaches the injection nozzle. A lateral movement of the screw produces a volumetric flow required during injection into a mold cavity. A schematic representation of the LPIM system in a mold alignment position is shown in Figure 1-6b (1) (Lamarre, Demers, & Chatelain, 2017). The injection sequence consists of the following steps: 1) Mixing under vacuum and pulling the injection cylinder downward to withdraw the desired volume of feedstock; 2) Alignment of the injection cylinder with the mold gate, slipping the sliding platform to cover the feedstock container, and exertion of mold holder pressure; 3) Displacement of the injection piston upward to inject feedstock into the mold cavity and 4) Releasing the mold holder pressure and removing the mold from the injection table to remove the solidified injection part (Figure 1-6b (2-7).

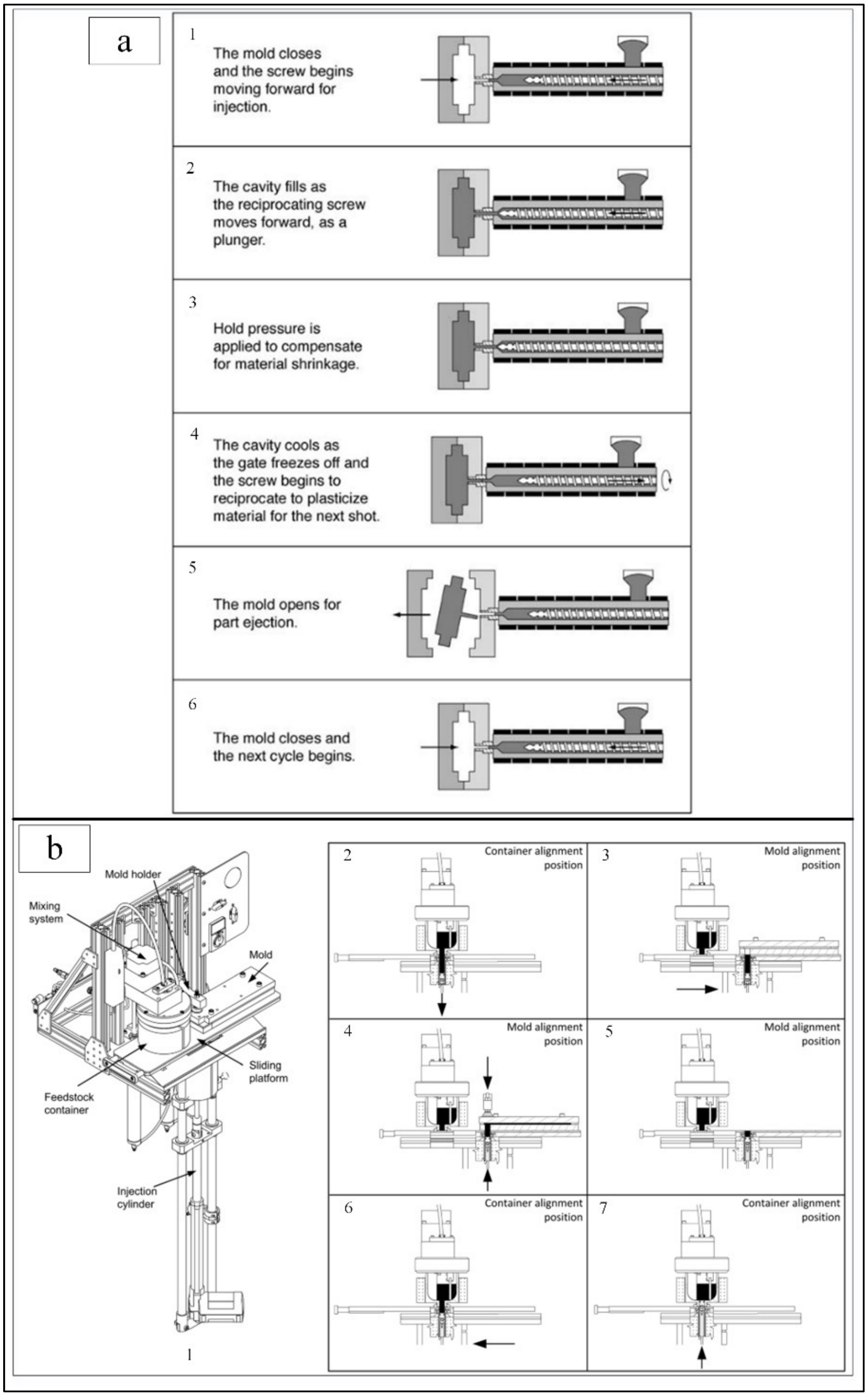

1 The mold closes and the screw begins moving forward for injection.

2 The cavity fills as the reciprocating screw moves forward, as a plunger.

3 Hold pressure is applied to compensate for material shrinkage.

4 The cavity cools as the gate freezes off and the screw begins to reciprocate to plasticize material for the next shot.

5 The mold opens for part ejection.

6 The mold closes and the next cycle begins.

a
b
Mold holder
Mixing system
Mold
Sliding platform
Feedstock container
Injection cylinder
1
2
Container alignment position
3
Mold alignment position
4
Mold alignment position
5
Mold alignment position
6
Container alignment position
7
Container alignment position

Figure 1-6 General view of the (a) HPIM taken from Donald F Heaney (2012, p. 119), and (b) LPIM injection molding machines taken from Lamarre et al. (2017, p. 2597)

1.5 Debinding

This step aims to extract partially or completely the binders from the green component using mainly three approaches. In thermal debinding, the green parts are heated up to the polymers' decomposition temperature. In solvent debinding, the injected components are immersed in a solvent to dissolve the carrier binder and leave the backbone in place for subsequent handling. In the catalytic debinding method, compacts are heated in an atmosphere containing catalysts to depolymerize and remove the polymers (Atre et al., 1998; D.F. Heaney, 2019). Following any debinding routes, the part becomes very brittle in this specific state before the last sintering processing step. The particle size, powder packing arrangement, binder viscosity, powder-binder interaction, debinding atmosphere, pressure in the chamber, heating rate, pre-sintering temperature, and the cooling rate can influence the debinding rate and overall quality of the debound parts (González-gutiérrez, Stringari, & Emri, 2012).

In the HPIM process, binders are generally removed in two stages using a solvent/thermal debinding approach. As illustrated in Figure 1-7a-b, low-molecular-weight constituents (i.e., carrier + surfactant) are initially dissolved in water or chemical solvents, using different debinding techniques, such as solvent extraction, direct sublimation, or evaporation, in which high-molecular-weight binder (e.g., polyethylene, polypropylene, etc. corresponding to 5-10% of the initial total binder volume, Figure 1-7c) acts as a backbone to keep the shape of debound components, and it is thermally decomposed during the early stage of the sintering cycle (A. C. Gonçalves, 2001). As shown in Figure 1-7d, minor particle bonding can also occur in the components after the debinding process.

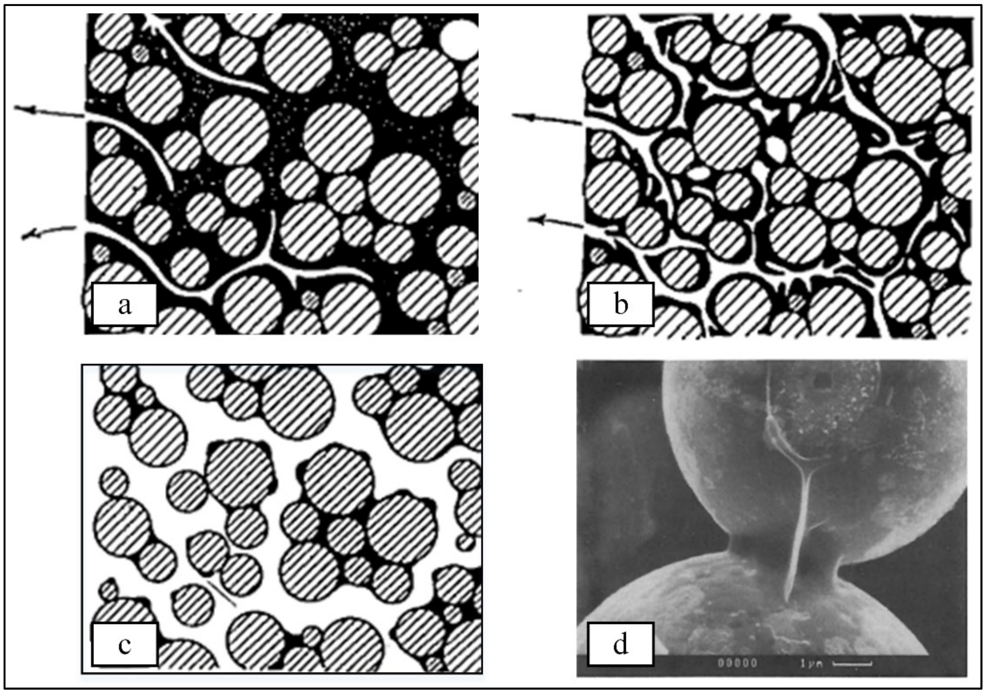

Figure 1-7 Schematic of binder distributions in two-stage debinding presenting the condition of binders (a) during solvent debinding stage, (b) at the beginning of the thermal debinding stage, (c) halfway through thermal debinding, and (d) example of two particles partially bonded (also known as the pre-sintered condition) after the debinding stage taken from Hwang, Lin, & Lee (1997, p. 604); Vervoort et al. (1996, p. 136)

In the LPIM process, binders are removed during a one-step thermal debinding. In this way, the injected parts are embedded into the wicking material (e.g., alumina, graphite, silica, clay, zirconia, or other fine powders), where all the binders are extracted by capillary forces during thermal debinding (e.g., at a temperature range between 200°C and 250°C) under vacuum or inert gas atmosphere. As illustrated in Figure 1-8, capillary suction promotes the binder movement from the parts toward the wicking agent. After that, the parts are heated up to a temperature less than the melting point of powders (also known as pre-sintering temperature) to start solid-state diffusion between metallic particles and obtain a minimum strength required for handling the parts through the sintering stage.

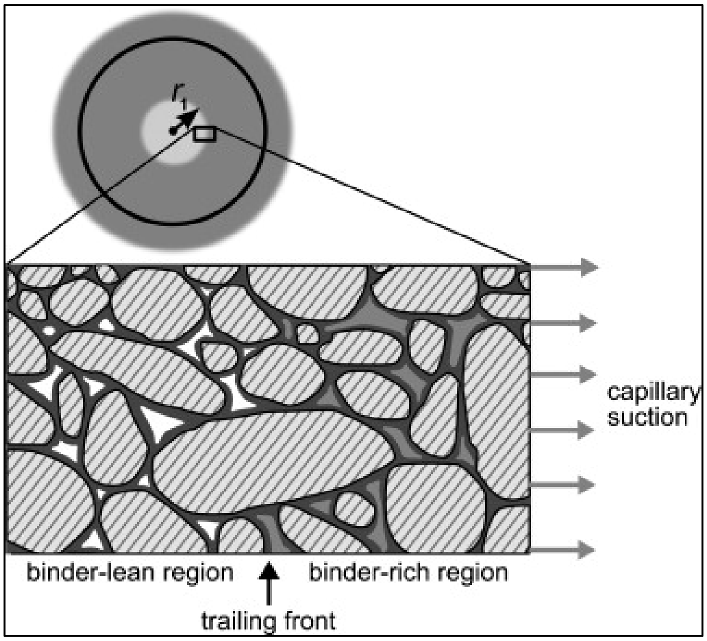

Figure 1-8 A schematic representation of the binder distribution during thermal wick-debinding taken from Gorjan, Dakskobler, & kosmač (2010, p. 3016)

From a practical perspective, thermal wick-debinding offers few advantages, such as the faster and safer debinding, than other debinding routes. Specifically, the use of a wicking agent in LPIM for shape retention during the extraction of a molten binder remains a significant advantage as compared to the use of high-viscosity backbone polymers. As illustrated in Figure 1-9 for two LPIM parts, debinding using a wicking media reduces the defects including distortion, warping, cracking, and shape loss. Nevertheless, defining wick-debinding parameters such as the wicked media, debinding time, and temperature is essential to avoid undesirable reactions, compositional changes, incomplete binder removal, and adhesion or possible bonding of the wicking powder on the part surface (Gorjan, 2012).

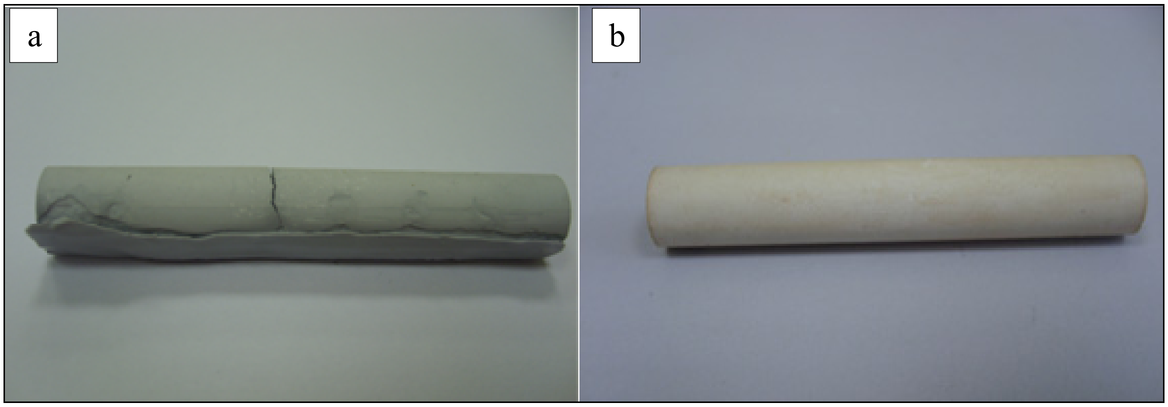

Figure 1-9 Low-pressure injection molded sample debound: (a) without wicking embedment using high-temperature debinding, and (b) with wicking embedded in highly porous alumina using low-temperature debinding taken from Gorjan (2012, p. 99)

Differential scanning calorimetry (DSC) and thermogravimetric analysis (TGA) are often used to assess the limits of the different process stages to design the debinding cycle. As shown in Figure 1-10a, the DSC graphs recorded during a heating cycle show different peaks corresponding to the melting points of each constituent (black arrows in Figure 1-10a). Therefore, the last peak is the melting point of the feedstock marked as T_m in Figure 1-10a that can be used to define the minimum temperature required for injection. Moreover, the TGA curve shows the evolution of the feedstock's weight during a heating cycle, where changes in the weight fraction represent the evolution of polymers' burnout. Thus, these values can be used to define the binder removal temperature (T_{D1} in Figure 1-10b) and burn-out temperature (T_{D2} in Figure 1-10b) to be used during the debinding cycle. Figure 1-10c presents an example of the typical debinding cycle for iron powders showing the debinding and pre-sintering plateaus.

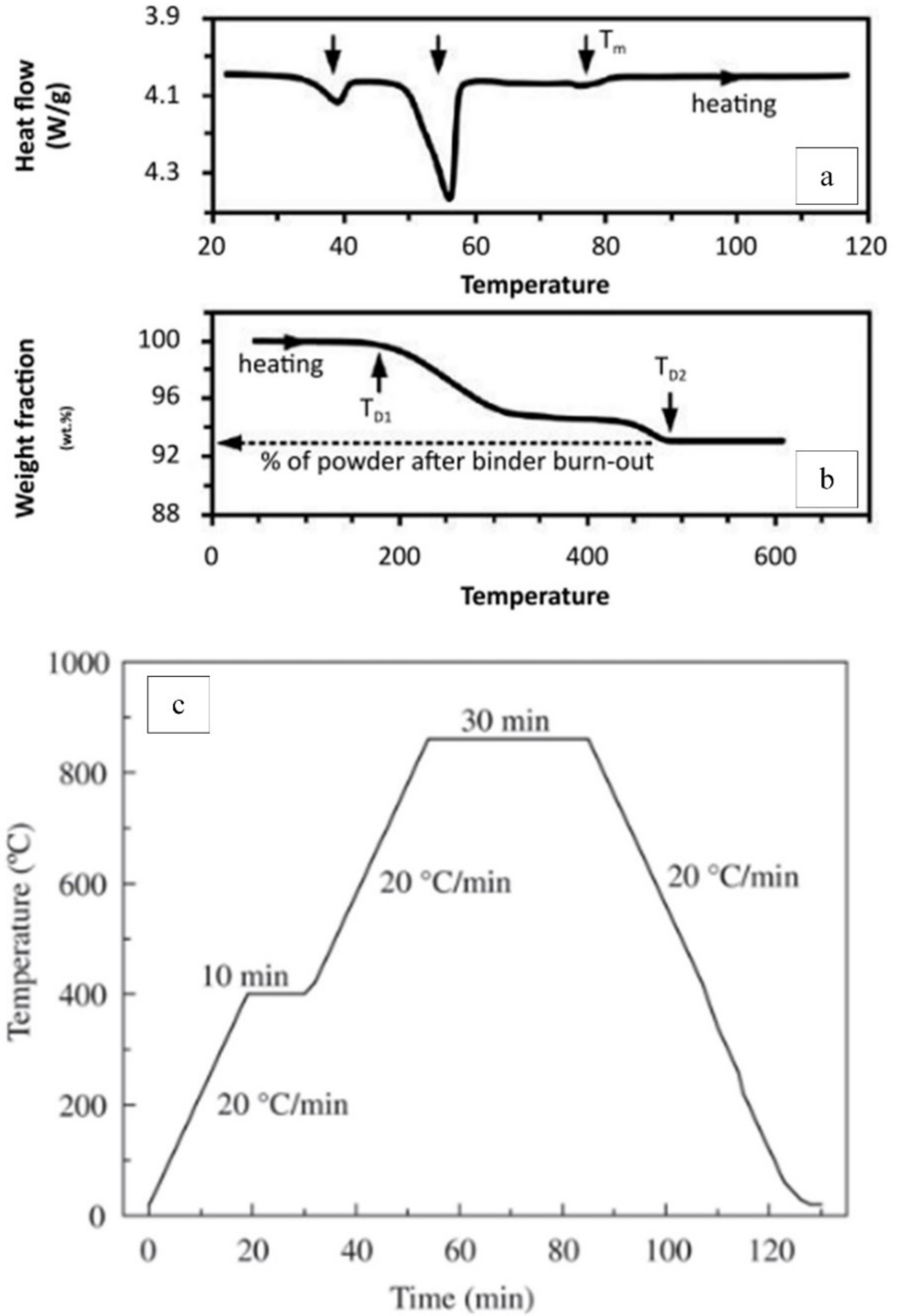

Figure 1-10 Thermal properties of wax-based feedstock obtained by (a) DSC, (b) TGA taken from Vincent Demers (2019, p. 60) and (c) typical thermal debinding and pre-sintering cycle for iron powder taken from Santos, Neivock, Maliska, Klein, & Muzart (2005, p. 510)

1.6 Sintering

The final stage in the PIM process consists of sintering, where debound components are heated up to a temperature close to the powder melting point to promote solid-state atom diffusion between powder particles (R. M. German, 2012; A. C. Gonçalves, 2001). In both the HPIM and LPIM processes, identical sintering cycles are used to achieve up to 95% of the theoretical density of components. As illustrated in Figure 1-11, After debinding, the powder network is similar to a loose powder state where the minor binding occurred after pre-sintering stage (Figure 1-11a) is transformed into inter-particle joints (Figure 1-11b and Figure 1-11c) that are later reorganized in a granular microstructure constituted of grains, grain boundaries, and pores (Figure 1-11d). The continuity of the material, the degree of porosity, and the shape of pores directly drive the mechanical properties of sintered components.

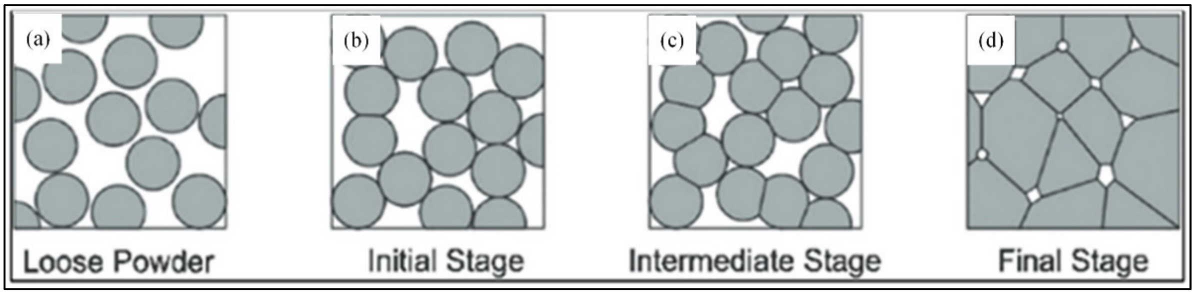

Figure 1-11 Evolution of the microstructure in sintering step in PIM involving the initial bonding of the particles followed by pore rounding and grain bounding and consequently final stage taken from Randall M German & Bose (1997, p. 226)

Due to the elimination of porosities between powders and bonding process a significant shrinkage of about 10 to 25% as compared to the green part is seen. Figure 1-12 illustrates injected, debound, and sintered parts fabricated from metallic powder feedstock, where this shrinkage is visible (Contreras et al., 2009; R. M. German, 2012; A. C. Gonçalves, 2001).

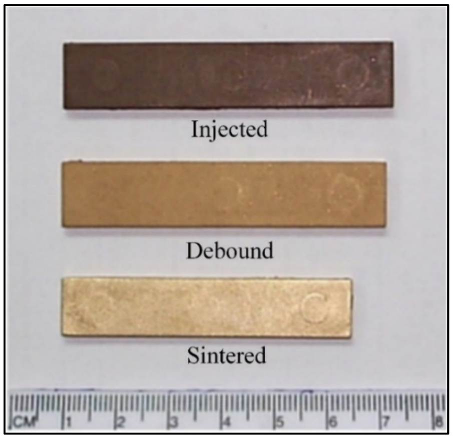

Figure 1-12 State of components prepared from bronze metallic feedstock taken from Contreras et al. (2009, p. 5620)

1.7 Properties of sintered component

The properties of sintered parts are influenced by various variables, including powder particle size, particle shape, and process parameters, and they are controlled to obtain suitable density and mechanical properties. Generally speaking, sintered parts exhibit monotonic mechanical properties close to that of the wrought material (e.g., up to 90% of the UTS), with a relative density varying between 95 and 98%. The post-sintering treatments may also improve the mechanical performance, the dimensional tolerance, or part esthetics, using hot isostatic pressing, machining, abrasive blasting, and polishing.

The microstructure of sintered samples used in HPIM is shown in Figure 1-13. This example reveals that the components produced with finer particles exhibit smaller spherical pores combined with smaller grains, all the features affecting sintered properties. Specifically, samples produced with -150 µm particles (-100 mesh, Figure 1-13a) generated numerous large interconnected pores and an average grain size of 90 µm. On the other hand, samples produced with -75 and -37 µm particles (-200 and -400 meshes, Figure 1-13b-c) exhibit nearly identical pore, but different grain sizes: about 65 and 40 µm, respectively. In this respect, sintered compacts prepared with a finer powder exhibit higher relative densities and tensile strengths, as illustrated in Figure 1-14 (Hu et al., 2018).

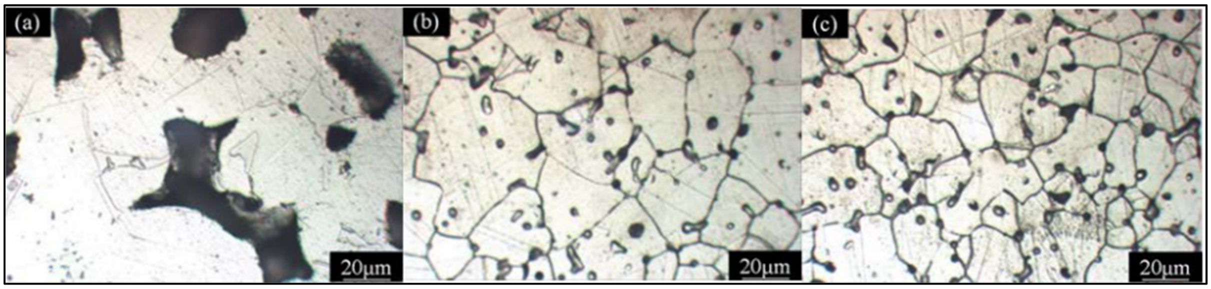

Figure 1-13 Microstructure of sintered components produced from irregularly-shaped stainless particles of different sizes: (a) -100 mesh powder, (b) -200 mesh powder; and (c) -400 mesh powder taken from Hu et al. (2018)

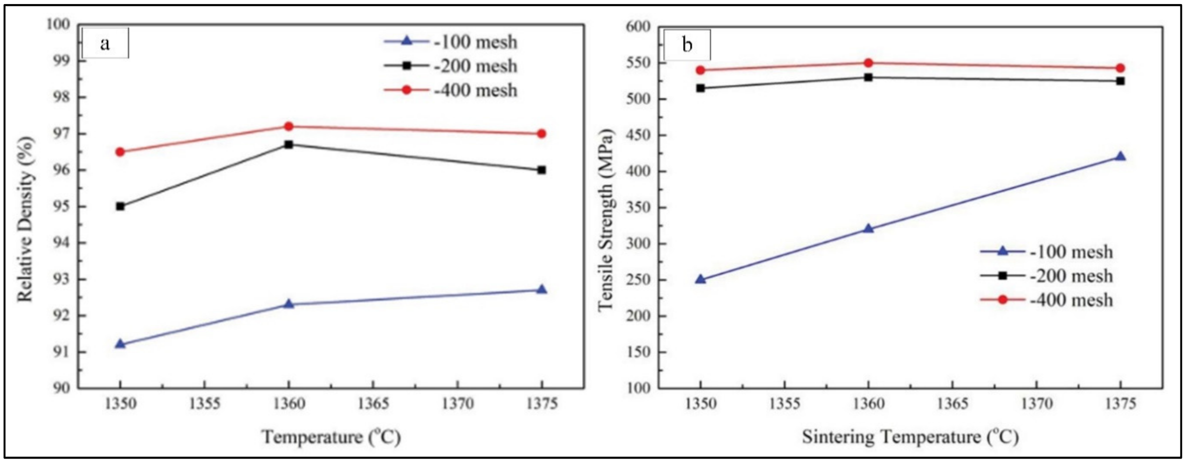

Figure 1-14 (a) Relative density (b) tensile strength of water-atomized stainless steel powders sintered at different temperatures taken from Hu et al. (2018)

Since particle shapes and sizes significantly influence the sintered properties, Contreras et al. (Contreras et al., 2009) studied these parameters for bronze-based feedstocks using a mixture of coarse irregular powders and fine spherical powders (Figure 1-15). They concluded that a relatively small increase in the fraction of irregularly-shaped particles negatively influences the density of injected parts and the debinding properties, but increases the relative density of sintered parts up to 95–97%. Figure 1-15 presents the relative density of the part after sintering at different temperatures, where Feedstock A containing only fine spherical powders achieved the highest density of 96% at a sintering temperature of 810 °C, while Feedstock G prepared with irregular coarse powders only reached a maximum density of 92% at 860°C. The rest of the parts presented density values ranging from 92 and 95% in the sintering temperature range of 830 to 860 °C. Both feedstocks B and E with 67% of spherical powders and 33% of irregular fine and coarse powders, respectively, reached a relative density of up to 95% at 830 °C, which is very close to the highest relative density of 96% obtained with Feedstock A.

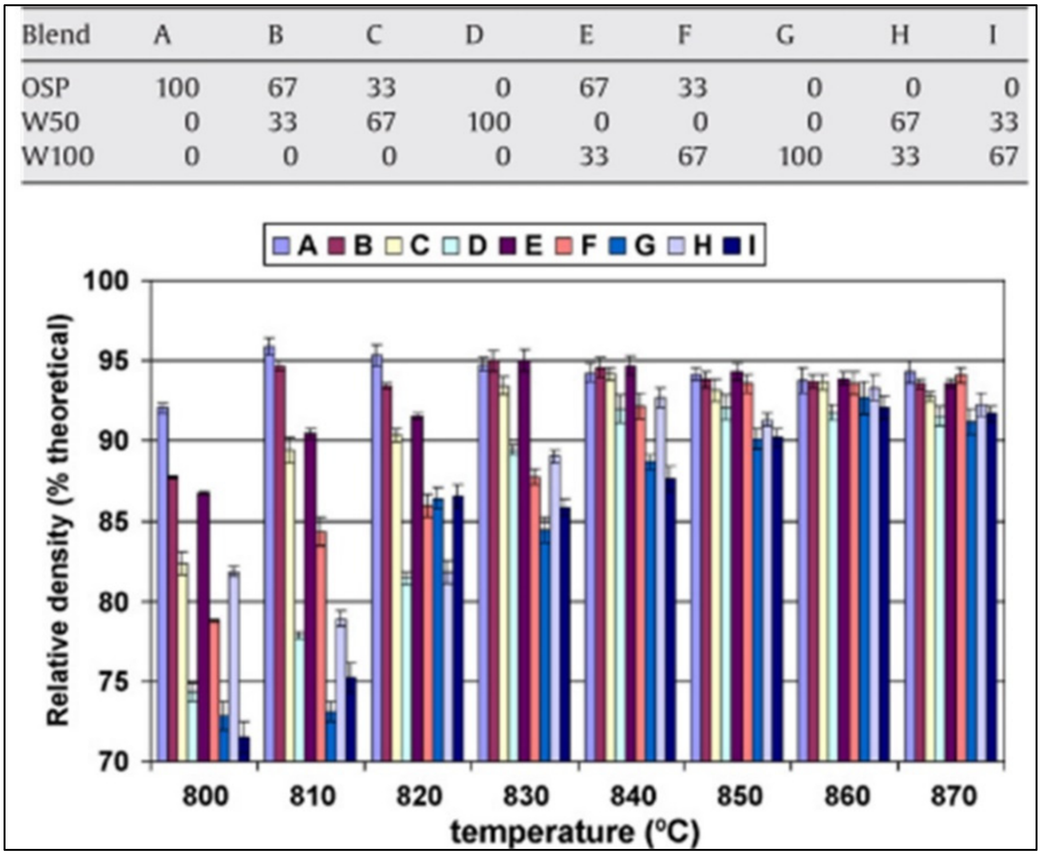

Blend	A	B	C	D	E	F	G	H	I
OSP	100	67	33	0	67	33	0	0	0
W50	0	33	67	100	0	0	0	67	33
W100	0	0	0	0	33	67	100	33	67

Figure 1-15 Influence of particle shape on the relative density of bronze sintered parts at different sintering temperatures taken from Contreras et al. (2009, p. 5623)

As complementary information, Table 1-2 summarizes the main conclusions about the influence of powder characteristics on the sintered properties of metallic parts produced by the HPIM process. In addition, more details on this specific topic are provided in the article presented in Chapter 4 of this thesis.

Table 1-2 Research studies on the influence of metal powder characterizations on properties of sintered components

Author	Metal or Alloy powders	Techniques	Main conclusion
Rane et al. (K. Rane & Date, 2019)	Iron oxide	HPIM	low-cost components can be produced by using recycled iron oxide despite the lower solid loading and sintered density
Mukund et al. (Mukund & Hausnerova, 2020)	Stainless steel	HPIM	An increase in the volume fraction of coarse powder and a decrease in the powder sphericity decrease the flow performance of feedstock and the sintered component properties
Ho et al. (Ho & Lin, 1995)	Stainless steel	HPIM	Finer powders decrease the moldability and result in developed microstructures and fewer interconnected pores of sintered parts; therefore, higher densities, mechanical properties were achieved

CHAPTER 2

PROBLEM DEFINITION AND RESEARCH OBJECTIVES

2.1 Problem definition

Based on the literature review, it is well known that the quality of final MIM components produced from metal powders depends on the powder characteristics (e.g., shape and size of particles) and binder constituents, feedstock formulation, injection conditions (e.g., temperature and pressure), debinding route, and sintering parameters. In recent years, the successful development of thermal debinding in conventional HPIM has been achieved using analytical or experimental models. However, and whatever the alloy, no study has been conducted on the final sintered properties of components produced from spherical or irregular metal powders using thermal wick-debinding adapted for the LPIM process. Specifically, the influence of characteristics of metallic irregular powders on the physical and microstructural properties has never been quantified for such low-cost powders used in LPIM process.

2.2 Research objectives

This work aims to investigate the capability of spherical and irregular iron-based LPIM feedstocks to be injected, debound, and sintered to produce dense iron parts.

The specific objectives of the current project are:

- Determine the influence of powder shape and size on the critical and maximum solid loadings
- Confirm the viscosity of irregular particle shape iron-based feedstocks based on LPIM criterion
- Demonstrate the capability of using thermal wick-debinding cycle for low-viscosity iron-based feedstocks
- Quantify the physical and microstructural properties such as density of iron components
- Confirm the expected trends where high density is generally obtained for finer and high sphericity powders

CHAPTER 3

EXPERIMENTAL METHODOLOGY

This chapter presents the experimental procedures for mixing, injecting, debinding, and sintering the iron-based feedstocks used in this project. The four step required to produce a MIM part are presented in Figure 3-1 and detailed below in this section. Other details are presented in the section “Experimental procedure” of the journal article presented in Chapter 4.

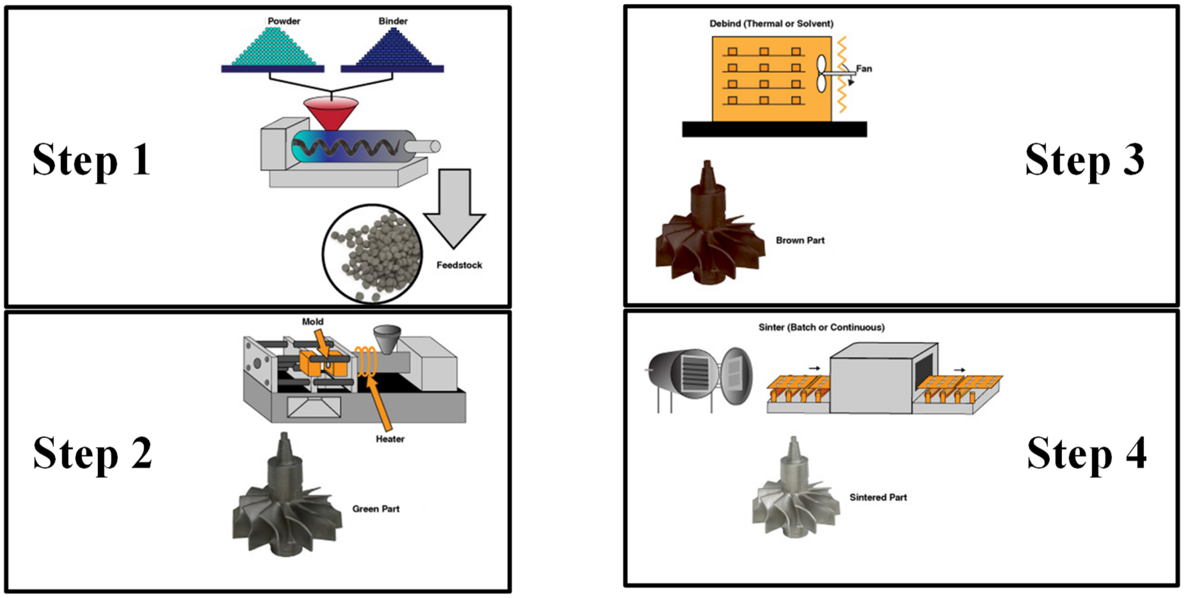
Step 1
Powder
Binder
Feedstock
Step 2
Mold
Heater
Green Part
Debind (Thermal or Solvent)
Fan
Step 3
Brown Part
Sinter (Batch or Continuous)
Step 4
Sintered Part

Figure 3-1 The four step required to produce a MIM part

3.1 Feedstock formulations

In this project, four different feedstocks were prepared from three irregular powder lots sieved with three mesh sizes labeled as -10 µm, -20 µm, and -45 µm, and one spherical carbonyl iron powder lot (CIP) with D_{50} of 4 µm. A scanning electron microscope (Hitachi 3600, secondary electron detector) and a laser diffraction particle sizing analyzer (Beckman Coulter LS13 320) were used to evaluate the powder morphology and quantify the particle size distribution. The four feedstocks were prepared using the same low-viscosity binder formulation constituted from a filler material (paraffin wax: PW), a demolding agent (carnauba wax: CW), a surfactant agent (stearic acid: SA), and a thickening agent (ethylene-vinyl acetate: EVA) illustrated in Figure 3-2. PW and CW are common waxes available in the form of blocks and flakes widely used in LPIM, while SA and EVA in the form of flakes and granules were used respectively to enhance the homogeneity of the feedstock as well as to prevent the powder-binder segregation phenomenon.

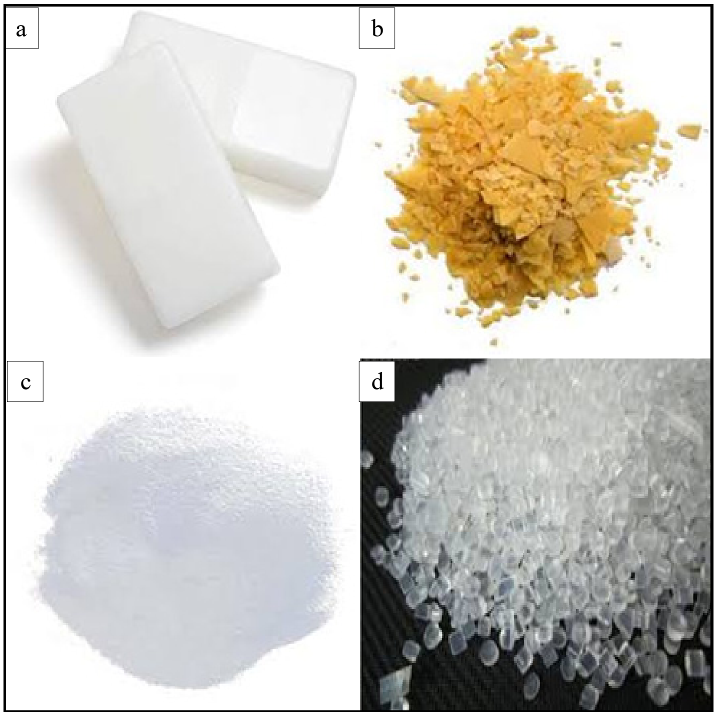

Figure 3-2 The appearance of the binders at room temperature a) paraffin wax, b) carnauba wax, c) stearic acid, and d) ethylene-vinyl acetate

The mixing process starts by weighting an exact mass of the powder and binders at room temperature using a precision balance. All constituents were then heated up to 110°C, cooled down at 80°C, and blended for 2 hours using the setup shown in Figure 3-3a. The mixtures were finally transferred to a vacuum container illustrated in Figure 3-3b for 2 hours at the same temperature of 80°C to remove all the microbubbles that might have been created inside the feedstock during mixing.

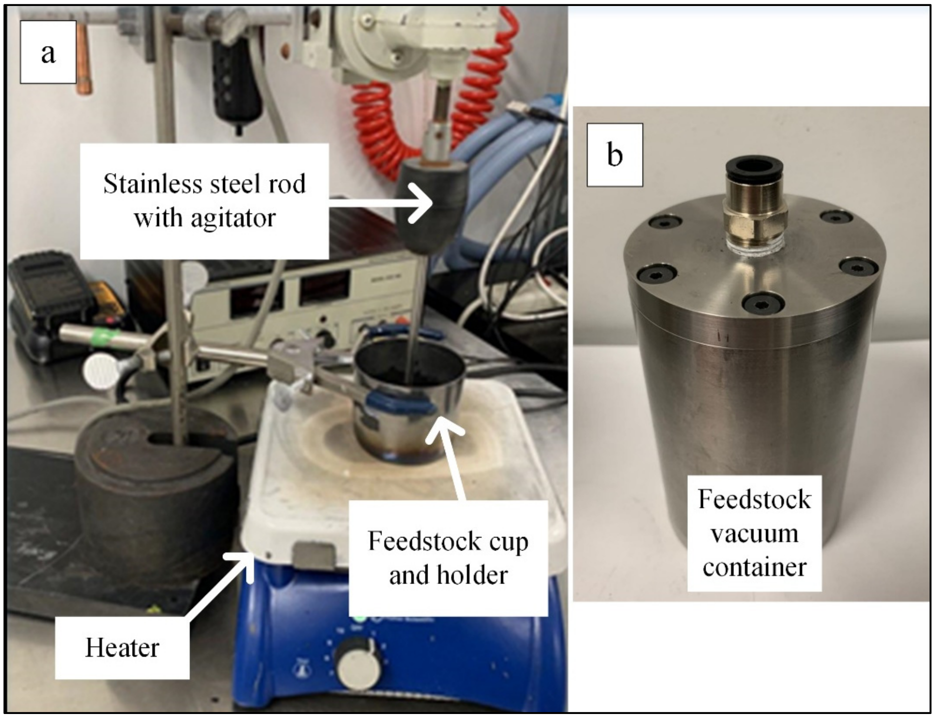
a
Stainless steel rod with agitator
Feedstock cup and holder
Heater
b
Feedstock vacuum container

Figure 3-3 a) Feedstock mixture and b) vacuum container

3.2 Feedstocks characterization

This section is dedicated to explaining the experimental methodology used to obtain all the feedstock physical, thermal, and rheological properties.

3.2.1 Measuring density and critical solid loading

The density of the metallic powder, binders, and feedstocks were obtained using a helium gas pycnometer (AccuPyc II 1340) depicted in Figure 3-4 according to ASTM B923-16 standard (ASTM International, 2016). The feedstock density was measured at different solid loadings and compared to the theoretical density values to determine the critical and maximum solid loadings for each powder-binder mixture.

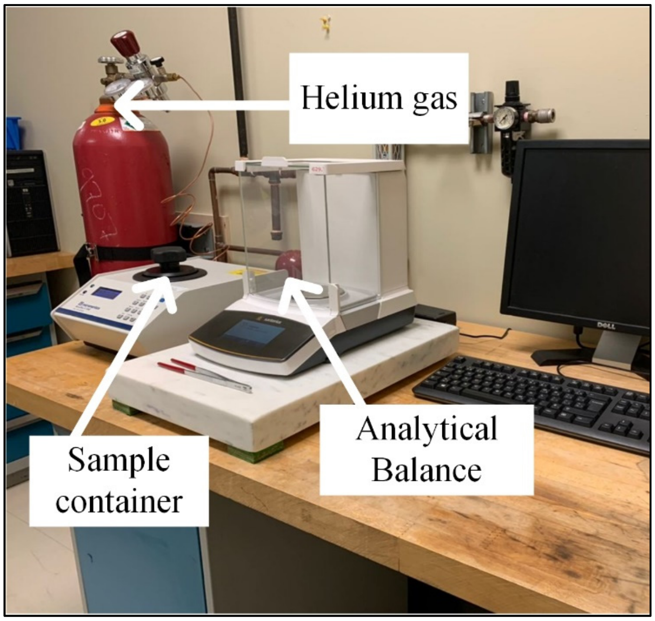

Figure 3-4 Pycnometer machine

3.2.2 Measuring the melting point and decomposition of binders and feedstocks

The melting points of binders and feedstock were obtained using a differential scanning calorimeter (DSC, Perkin Elmer) shown in Figure 3-5. Feedstock samples with a mass of about 10 mg were encapsulated in the aluminum hermetic pans, placed in the DSC before applying the heating/cooling cycles. Two thermal cycles from 20 to 120°C at 10°C/min under a dry nitrogen gas flow of 50 ml/min were used to obtain DSC thermograms of the second heating cycle. The last peak obtained during the heating cycle was used to calculate the feedstock melting point.

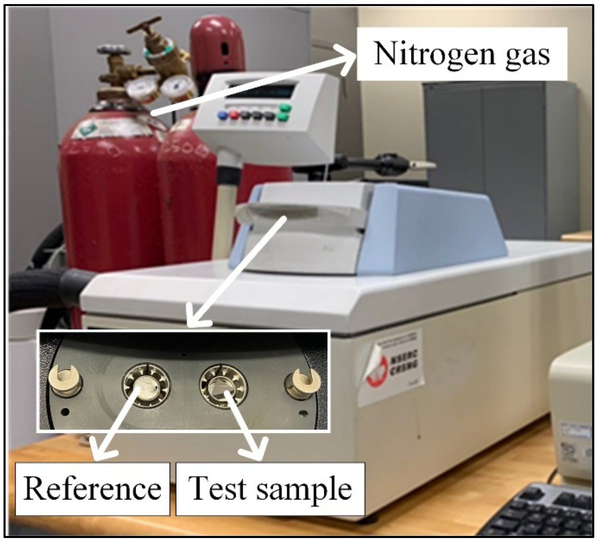
Nitrogen gas
Reference
Test sample

Figure 3-5 DSC equipment

The start and end binder degradation temperatures were assessed using a thermogravimetric analyzer (TGA, Pyris Diamond TG/DTA) illustrated in Figure 3-6. A 1 mm^3 sample was extracted from an injected part before being placed in a standard platinum pan and heated from 20 to 600°C at 20°C/min under high purity nitrogen purge gas with 60 ml/min flow rate.

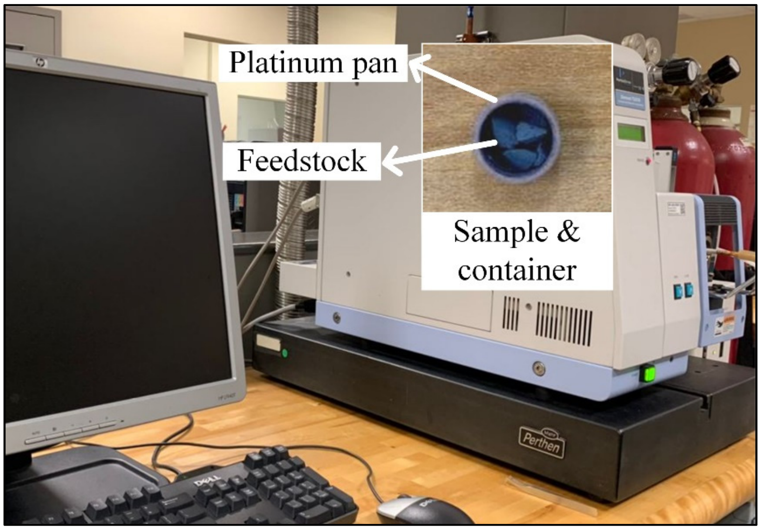
Platinum pan
Feedstock
Sample &
container

Figure 3-6 TGA equipment

3.2.3 Measuring viscosity

Viscosity profiles of the four feedstock were obtained using a rotational rheometer (Anton Paar MCR 302) illustrated in Figure 3-7a equipped with a concentric-cylinder cell (C-PTD 200) schematized in Figure 3-7b and a Peltier temperature-controlled system. The viscosity profiles were obtained at 80°C for shear rates ranging from 0.5 to 500 s^{-1}. The feedstock, the cylinder, and the container were preheated at the testing temperature to prevent the potential segregation during the test with low-viscosity feedstocks.

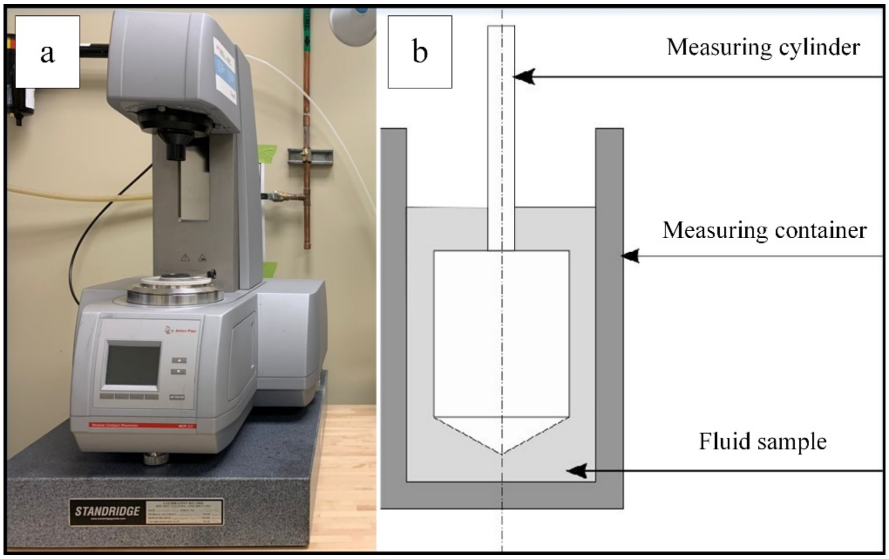

Figure 3-7 a) Rheometer equipped with a Peltier temperature-controlled system b) cross-section of the concentric-cylinder cell

3.3 Injection process

Rectangular specimens were injected using a low-pressure injection machine shown in Figure 3-8a. The feedstock was heated up at 80°C, blended, poured into the injection cylinder, and injected into the steel mold cavity illustrated in Figure 3-8(b-c). To facilitate the demolding operation, the rectangular mold was kept at 40°C during the injection process.

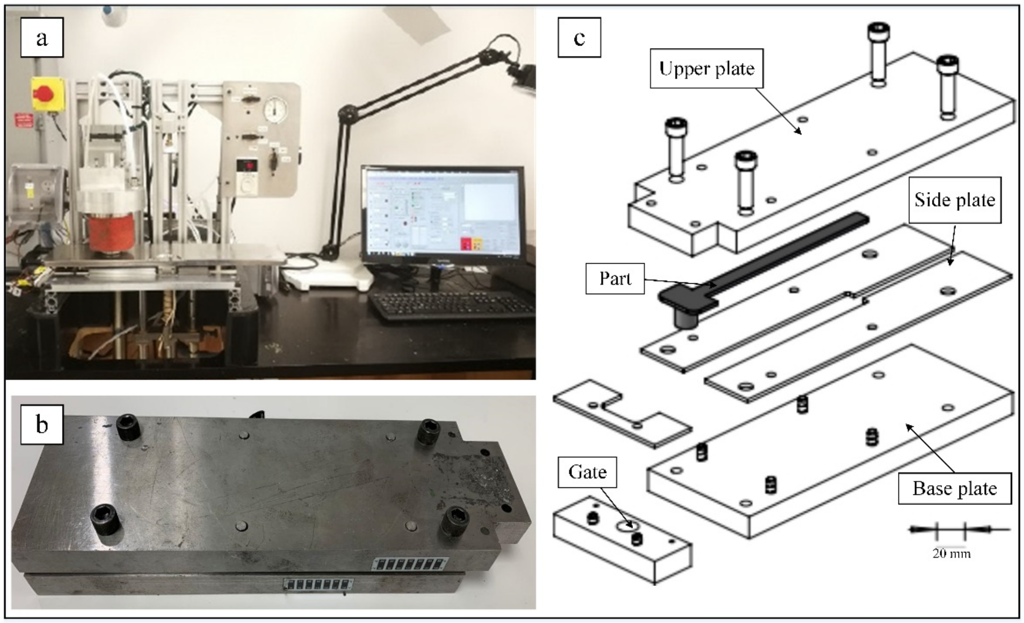

Figure 3-8 a) Exploded view of the rectangular mold, b) rectangular steel mold, and c) low-pressure injection machine

3.4 Debinding and sintering cycles

The injected parts were settled on an alumina powder bed in a metallic boat and buried under loose alumina powders that were slightly compacted using a flat tool to prevent any slump or deflection of samples. Alumina powders were sieved using a standard mesh #18 and a vibration machine to minimize powder agglomeration. The boats were placed in a metallic retort, and the air was pumped out from the retort using a vacuum pump and replaced with argon gas with a flow rate of 15 L/min. This procedure was repeated six times to guarantee that the retort is filled up with argon gas. The retort was finally introduced in a Nabertherm N 41/H furnace (Figure 3-9a) and heated up to 650°C during a total cycle time of about 23 hours. Subsequently, debound components were taken out of the boat and air cleaned to remove alumina powder before being sintered at 1250°C for 90 minutes under pure hydrogen using a CM furnace model 1516 (Figure 3-9b).

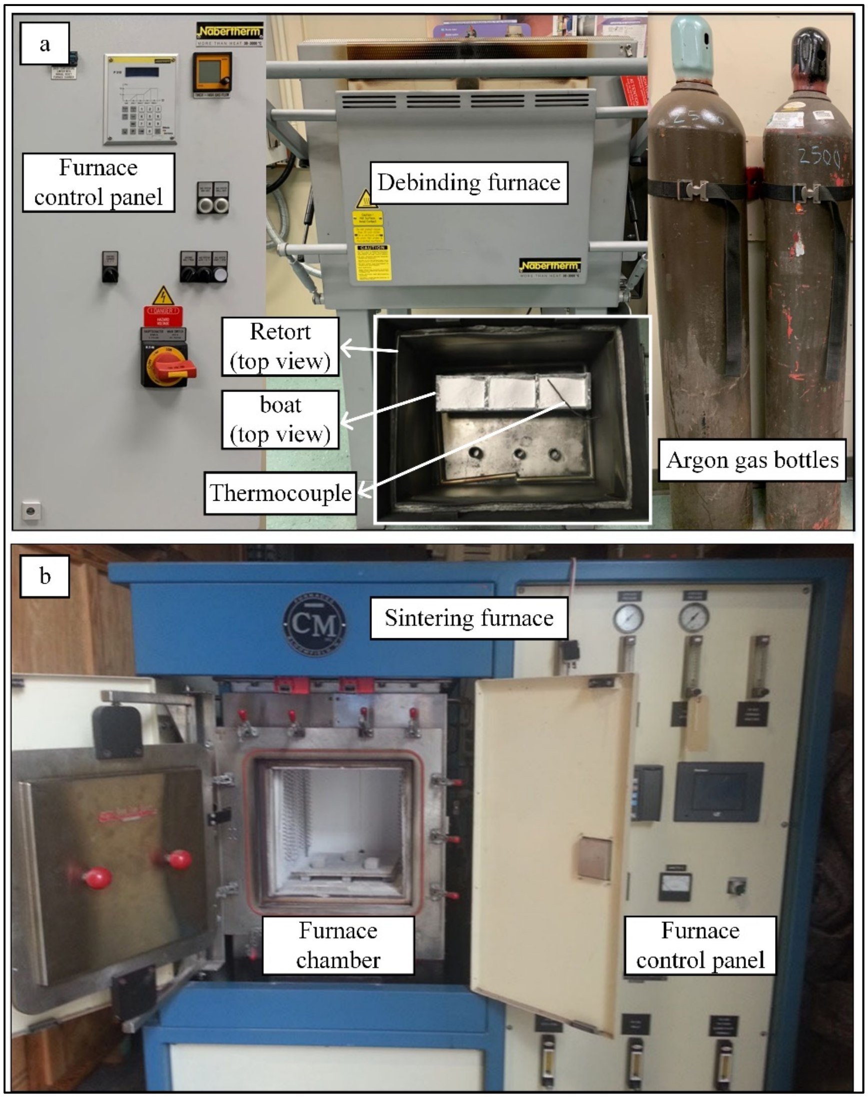
a
Furnace control panel
Debinding furnace
Retort (top view)
boat (top view)
Thermocouple
Argon gas bottles
b
Sintering furnace
Furnace chamber
Furnace control panel

Figure 3-9 Overview of a) debinding and b) sintering furnaces setup

3.5 Characterization of the debound and sintered properties

Debound specimens were observed using a scanning electron microscope (SEM S3600-N Hitachi) as shown in Figure 3-10 to characterize the debound powder network (channels, bonding, distribution of particles, and clusters) and assess a possible presence of remaining binders.

Figure 3-10 Scanning electron microscope

The density of sintered specimens was measured using the oil-impregnation method based on Archimedes' principle according to the MPIF standard 42 (MPIF Standard, 1986) using the setup presented in Figure 3-11. The sintered samples were dry weighed (by Sartorius weighing balance) using the upper plateau and then soaked in oil for 4 hours under vacuum before being weighted again using the upper plateau. The oil-impregnated samples were finally weighed in distilled water at 22.5°C before calculating the sintered density using Equation 3.1

$$\rho_s = \frac{A * \rho_w}{B - C} \quad (3.1)$$

where ρ_s is the sintered density (g/cm^3), A is the dry mass of the sintered sample (g), ρ_w is the water density at test temperature (g/cm^3), B is the mass of the oil-impregnated sample (g) in air, and C is the mass of the oil-impregnated sample (g) in water.

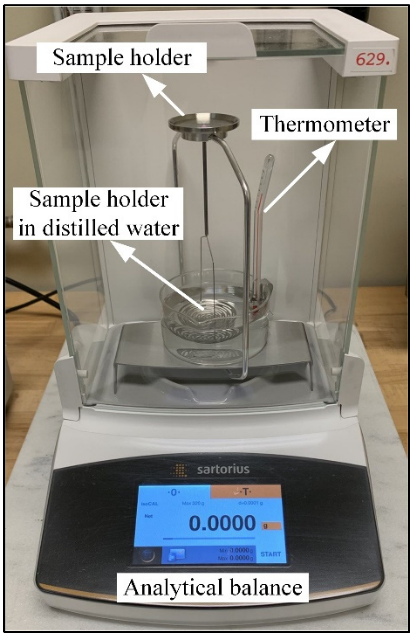
Sample holder
629.
Thermometer
Sample holder
in distilled water
sartorius
0.0000
Analytical balance

Figure 3-11 Archimedes' density measurement setup

The metallographic observations were performed on cross-sections of the sintered specimens using an optical microscope (Olympus GX51) illustrated in Figure 3-12a. The sintered parts were vacuum-impregnated with epoxy resin and cured at 60°C as illustrated in Figure 3-12b or Bakelite mounted using a semi-automatic machine (Struers Labopress) shown in Figure 3-12c, and finally mirror-polished using an automatic polishing machine (Buehler Motopol 2000) presented in Figure 3-12d, using the polishing procedure presented in Table 3-1.

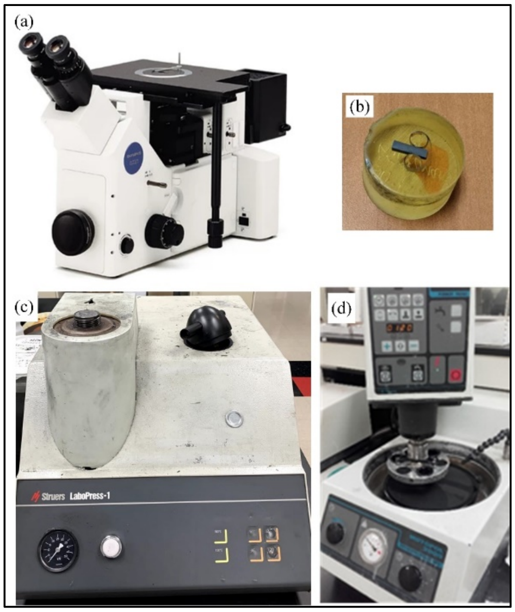

Figure 3-12 (a) Olympus GX51 inverted metallurgical microscope (b) mounted sample, (c) Struers Labopress semi-automatic machine, and (d) Buehler Motopol 2000 automatic polishing machine

Table 3-1 Standard protocol for polishing sintered samples

Sandpaper size (grit)	240	320	400	600	800	1 µm
Speed (rmp)	150	150	150	150	150	150
Strength (ibf *10)	0-5	5-10	5-10	5-10	5-10	5-10
Time (s)	80	80	80	120	120	120
Liquid	water	water	water	water	water	1 µm diamond suspension monocrystalline
Rotation direction	clockwise	clockwise	clockwise	clockwise	clockwise	counterclockwise

CHAPTER 4

EFFECT OF POWDER SHAPE AND SIZE ON THE PROPERTIES OF LOW VISCOSITY IRON-BASED FEEDSTOCK USED IN LOW-PRESSURE POWDER INJECTION MOLDING

Seyed Mohammad Majdi[a], Atefeh Ayatollahi Tafti[a], Vincent Demers[a], Guillem Vachon[b],
Vladimir Brailovski[a]

[a] École de technologie supérieure, 1100 Notre-Dame West, Montreal, H3C 1K3, Canada
[b] Rio Tinto Metal Powders, 1625 route Marie-Victorin, Sorel-Tracy, J3R 4R4, Canada

The results collected during this research project have been compiled to write an article constituting this chapter. This article was published in the journal "Powder Metallurgy". It will focus on the impact of powder shape and size of iron-based feedstock on physical and microstructural properties such as sintered density, debound network, and metallography of sintered parts.

4.1 Abstract

Low-pressure powder injection molding (LPIM) is a cost-effective manufacturing technology used to fabricate complex-shaped parts with high mechanical properties at low- or high-volume production. This research work presents an experimental approach to investigate the debound/sintered properties of iron components produced by the LPIM process using iron-based powders exhibiting different particle shapes and size distributions. Four low-viscosity feedstocks were mixed and injected into a rectangular mold cavity before being thermally wick-debound and finally sintered using identical debinding and sintering cycles. This study confirms that both irregular and spherical iron powders can be shaped via the LPIM process. The solid loadings obtained with these two powder morphologies, varying from 58 to 62 vol. %, represent expected values. Metallographic observations validated the trend in the density values obtained with irregular (~6.6 g/cm^3) and spherical (~7.5 g/cm^3) powders.

Keywords: Low-pressure powder injection molding (LPIM); thermal wick-debinding; pre-sintering temperature; sintering; iron powder; irregular particles.

4.2 Introduction

Metal injection molding (MIM) is a cost-effective near-net-shape manufacturing technique that combines the advantages of powder metallurgy and plastic injection molding technologies. In MIM, a molten polymeric binder is mixed with a metallic powder to produce a feedstock injected into a mold cavity, debound, and sintered to finally obtain dense parts (Atre et al., 1998; Donald F Heaney, 2018; Kryachek, 2004). Based on the binder system, the process is categorized as either high-pressure powder injection molding (HPIM) or low-pressure powder injection molding (LPIM). High-viscosity feedstocks (e.g., > 100 Pa·s) containing a backbone polymer generally require the conventional HPIM approach, which uses reciprocating screw machines to inject green parts at pressures ranging from 50 to 200 MPa (R M German, 1990; Mangels, 1994; Piotter et al., 2011; Ruprecht, Gietzelt, Müller, Piotter, & Haußelt, 2002). By contrast, as it takes advantage of low-viscosity feedstocks (e.g., < 20 Pa·s), the LPIM approach uses a plunger system or compressed gas principle to produce green parts using pressures varying from 0.1 to 1 MPa (Aparecido Carlos Gonçalves, 2001; Liberati et al., 2006; Zorzi, Perottoni, & Da Jornada, 2002). Although the binder system drives the mixing, injection, and debinding stages, the final sintered properties are primarily a function of the powder characteristics, such as the particle morphology, the particle size, and the particle size distribution (Koseski, Suri, Earhardt, German, & Kwon, 2005; Mamen, Song, Barriere, & Gelin, 2015). In MIM, fine spherical powders produced mainly by gas atomization or chemical decomposition with a D_{50}, which is generally < 20 µm, are routinely used to achieve higher packing densities, better flowability, higher solid loadings, and better sinterability, as compared to irregularly shaped powders (Ali & Ahmad, 2020; Hausnerova et al., 2017). However, powders containing coarse irregular particles typically produced by water atomization lead to a higher brown strength (i.e., the strength of the part after debinding), as compared to spherical powders, and allow the manufacture of larger complex shape components while reducing the overall production cost (Hashikawa, Osada, Kudo, Tsumori, & Miura, 2016; Park et al., 2009). Although the influence of particle size on the moldability, debindability, and sinterability of MIM components has been demonstrated for spherical powders (Dimitri, Mohamed, Thierry, & Jean-Claude, 2017; Sotomayor, Várez, & Levenfeld, 2010), the effect of this key parameter for irregular powders has only been addressed by a few research groups, all using high-viscosity feedstocks adapted for conventional HPIM technology. Hausnerova et al. (Hausnerová, Sáha, & Kubát, 1999) studied the effect of the particle size distribution (PSD) on the rheological behavior of two hard metal carbide irregular powder lots. They concluded that feedstocks formulated with a bi-modal PSD exhibit lower viscosities and higher solid loading capacities than those formulated with uni-modal PSD. Hu et al. (Hu et al., 2018) explored the fabrication of MIM parts using three irregular-shaped water atomized stainless steel powders ($19 < D_{50} < 66$ µm). They confirmed that while the feedstocks prepared with finer powders decrease the moldability, their sintering results in parts with well-developed microstructures and fewer interconnected pores, and therefore, with higher densities, enhanced mechanical properties, and better corrosion resistance, as compared to coarser powders. Mukund et al. (Mukund & Hausnerova, 2020) investigated the effect of PSD on the feedstock viscosity, sintered properties, and dimensional stability of MIM components obtained from water atomized stainless steel powders with irregular and ligamental morphologies. They demonstrated that an increase in the volume fraction of coarse powders, as well as a decrease in the powder sphericity, decrease the flow performance of feedstocks and the overall sintered part quality.

Contreras et al. (Contreras et al., 2009) studied the effect of powder size and shape on the green strength, debinding, and sintering behavior of different bronze-based feedstocks prepared from a mixture of fine spherical gas atomized and coarse irregular water atomized powders at a ratio of 9:1, respectively. They determined that while the green strength is mostly driven by PSD, and not by particle morphology, an addition of irregular water atomized powders increase the tortuosity of the path through which the binder travels to leave the part, thus decreasing the debinding rate. Notwithstanding this last phenomenon, they obtained sintered densities and mechanical properties similar to those of parts produced from only fine spherical gas atomized powders. Similarly, Shu and Hwang (Shu & Hwang, 2004) used different iron-based powder mixtures constituted from coarse irregular (water atomized) and fine spherical (chemically decomposed) powders to investigate the effect of particle size and shape on the feedstock moldability and powder sinterability. They concluded that replacing fine spherical powders with coarse irregular powders (ratio of 6:4) does not significantly change the molding and debinding behavior of iron-based feedstocks. On the other hand, adding small quantities of α-phase stabilizers, such as P and Mo, minimizes the grain growth and improves the relative sintered density up to 96%, even for a powder mixture containing up to 60 wt. % of coarse irregular powders. Equally, in a bid to lower the raw material costs by using irregular powders, some research groups also explored the fabrication of MIM parts using recycled materials. In this context, Rane and Date (K. K. Rane & Date, 2014) investigated the rheological behavior of two feedstocks, one prepared from irregular-shaped fine powders produced by grinding sludge, and another one obtained by blending the first powder with fine graphite flakes. They confirmed that feedstock formulated with only recycled powder manifests low flowability due to high inter-particle friction inherent to the powder shape, while the addition of graphite flakes decreases the viscosity and improves the moldability of such low-cost feedstocks. A few years later, the same research group confirmed that recycled iron oxide powders can potentially be used in the production of low-cost MIM components despite lower achievable solid loadings and sintered densities as compared to virgin powders (K. Rane & Date, 2019).

Notwithstanding the efforts mentioned above, the fabrication of MIM parts from irregular metallic-based feedstocks has generally been realized using only the HPIM route, while the use of such irregular powders in the LPIM process has never been demonstrated. To start filling this gap, this work aims to study the effect of powder shape and size on the sintered density of iron-based components produced using the LPIM processing route.

4.3 Experimental procedure

4.3.1 Materials and feedstock characterization

Four different feedstocks were prepared using three irregular iron powder lots provided by Rio Tinto Metal Powders (Sorel-Tracy, Canada) and one spherical powder lot. Irregular powders were produced using a three-step workflow comprising water atomization, high-energy milling, and sieving with three mesh sizes: -45 µm, -20 µm, and -10 µm. The spherical powder produced by carbonyl iron powder was referenced as CIP. A scanning electron microscope (Hitachi 3600, secondary electron detector) and a laser diffraction particle size analyzer (Beckman Coulter LS13 320) were used to evaluate the powder morphology and quantify the particle size distribution, respectively. The -45 µm, -20 µm, and -10 µm powder lots exhibited irregular and angular morphologies generally expected of powders produced using this powder fabrication workflow (Figure 4-1 (a-c)), while the CIP showed a mixture of spherical and near-spherical particles typical for this fabrication route (Figure 4-1d). The frequency and cumulative particle size distributions plotted in Figure 4-1 (e-h) were used to extract the powder characteristics such as D_{10}, D_{50}, and D_{90}, as reported in Table 4-1. The density of the metallic powders and binders, as well as the maximum solid loading of each feedstock, were measured using a helium gas pycnometer (AccuPyc II 1340) according to the ASTM B923-16 standard (ASTM International, 2016).

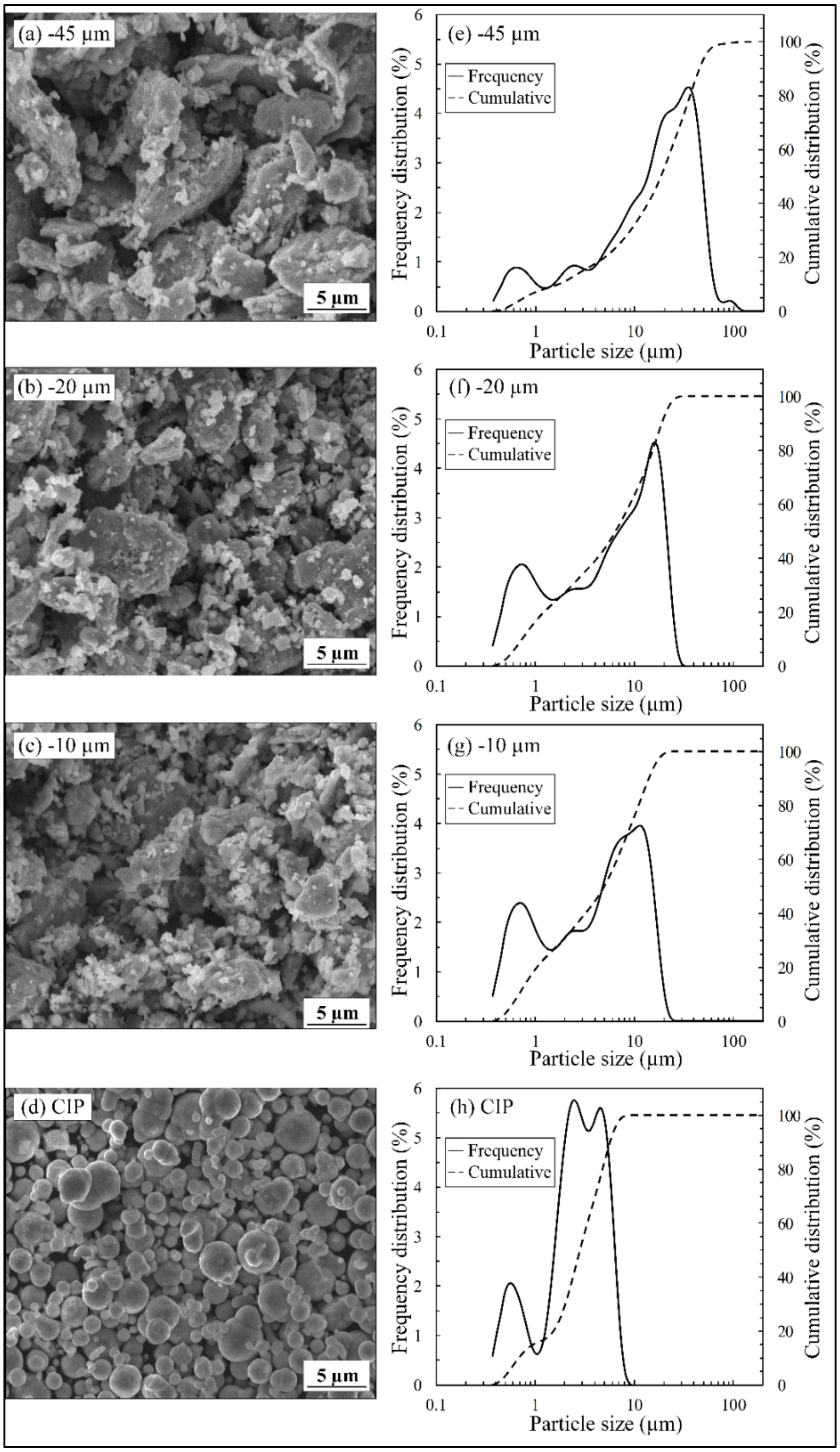

Figure 4-1 SEM micrographs and particle size distributions of four iron-based powder lots: (a, e) -45 μm, (b, f) -20 μm, (c, g) -10 μm, and (d, h) CIP

Table 4-1 Characteristics of iron powders

Powder identification	Shape	D_{10} (µm)	D_{50} (µm)	D_{90} (µm)	Density (g/cm^3)
-45 µm	Irregular	1.9	18.3	44.9	7.4
-20 µm	Irregular	0.7	6.5	19.0	7.1
-10 µm	Irregular	0.7	5.0	14.1	6.9
CIP	Spherical	1.8	4.0	7.7	7.5

The binders were formulated from a blend of paraffin wax (PW) used as the base constituent, and three other additives, including stearic acid (SA), used as a surfactant agent, carnauba wax (CW) used as a shrinking agent, and ethylene-vinyl acetate (EVA) used as a thickening agent, with the characteristics reported in Table 4-2. These constituents were selected based on their extensive use in the LPIM process (Amin, Jamaludin, & Muhamad, 2009; V. Demers, Turenne, & Scalzo, 2015; Rei, Milke, Gomes, Schaeffer, & Souza, 2002). Four feedstocks were formulated from the four iron powder lots using similar binder proportions at the maximum solid loadings value for each powder lot. Based on recent works on similar water atomized iron-based powders (Tafti, Demers, Vachon, & Brailovski, 2021), the binder proportion was set at 1 vol. % of SA, 2 vol. % of CW, 2 vol. % of EVA, and the balance of PW, to create adequate surfactant, demolding, and thickening effects. Dry powders were mixed in a laboratory mixer with the molten binders for 4 hours at 80°C under a vacuum to remove micro-bubbles from the feedstock. Differential scanning calorimetry (DSC) analyses were conducted using a Perkin Elmer Pyris 1 DSC to evaluate the melting points of the binder constituents and feedstocks according to the ASTM D3418-15 standard (ASTM International, 2015). To this end, feedstock samples with a mass of around 10 mg were encapsulated in standard aluminum hermetic pans before performing two sequential temperature scans from 30 to 100°C with a heating rate of 10°C/min and dry nitrogen gas flow of 50 ml/min. The DSC thermograms were recorded from the second heating cycle to minimize the influence of thermal history and maximize the thermal contact between the pan and the specimen.

Table 4-2 Characteristics of binder constituents

Constituent of binders	Melting point (°C)	Density (g/cm^3)	Supplier
Paraffin wax (PW)	59.0	0.9	Sigma-Aldrich
Carnauba wax (CW)	84.5	1.0	Sigma-Aldrich
Stearic acid (SA)	75.0	0.9	Sigma-Aldrich
Ethylene-vinyl acetate (EVA)	49.0	1.0	Sigma-Aldrich

The viscosity profiles of the four feedstocks were obtained using an Anton Paar MCR 302 rotational rheometer equipped with a concentric cylinder cell (CC17) and a Peltier temperature-controlled system (C-PTD200). The profiles were obtained at a constant temperature of 80°C for shear deformation rates ranging from 0.5 to 500 s^{-1}. To prevent potential segregation potentially arising during the tests, the feedstock, cylinder, and container were pre-heated to the testing temperature according to the procedure developed in (Fareh, Demers, Demarquette, Turenne, & Scalzo, 2017). A thermogravimetric analysis (TGA) was performed using a PerkinElmer STA 8000 to measure the initial and final binder decomposition temperatures. To this end, a specimen of about 1 mm^3 was extracted from the injected parts, placed in a standard ceramic pan, and heated from 50 to 550°C using a heating rate of 20°C/min under high purity argon purge gas at a flow rate of 50 ml/min.

4.3.2 Injection, debinding, and sintering

The LPIM injection press presented in Figure 4-2a was used to inject each feedstock into the rectangular mold cavity illustrated in Figure 4-2b. The rectangular green parts (165 × 12.5 × 3 mm) were produced using a constant volumetric flow rate of 2.2 cm3/s to generate a maximum injection pressure of about 0.5 MPa, with a feedstock temperature maintained at 80°C, and a mold temperature set at 40°C.

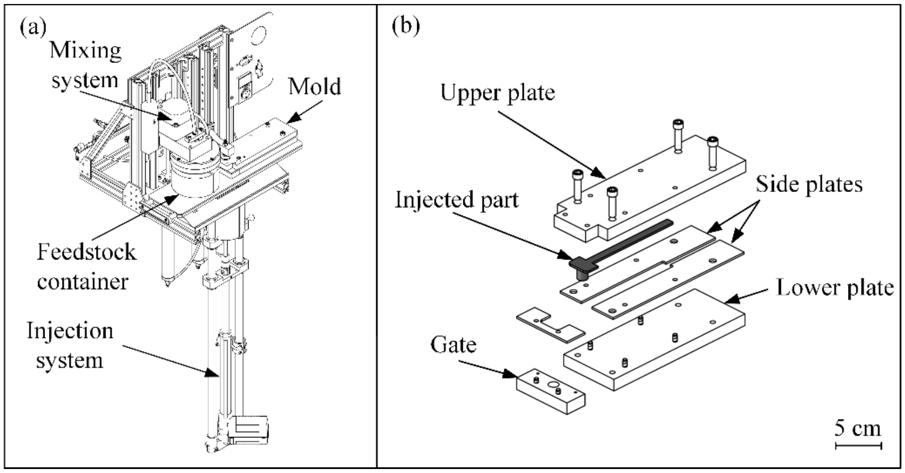

Figure 4-2 (a) Schematic view of the LPIM injection press, and (b) exploded view of the rectangular mold used during injections

The green parts were then settled on an alpha-phase 99.9% alumina powder bed (provided by Alfa Aesar, Thermo Fisher Scientific, lot # 42572), compacted in a metallic boat illustrated in Table 4-3a, before being buried in loose alumina powder, as shown in Figure 4-3b. This inert alumina powder was used as a wicking medium during the debinding stage as well as to support the parts before the pre-sintering stage. Metallic boats containing the parts and alumina powder bed were placed into a tight metallic retort in which air was removed using a vacuum pump and replaced with a continuous 15 l/min argon gas flow throughout the debinding pre-sintering cycle. The retort was introduced into the Nabertherm N 41/H debinding furnace to perform the thermal wick-debinding cycle developed in this work. Since the design of a debinding cycle is an important segment of the present work, all details are available in the Results and discussion section.

Following the debinding treatment, the brown parts were removed from the boat, and air-cleaned to remove alumina powder. One part per powder condition was broken to observe the bonding networks at different locations along the cross-section using a scanning electron microscope (Hitachi 3600, Secondary Electron Detector). The rest of the debound specimens were settled on a dense zirconia plate and sintered in a high-temperature CM Furnace (model 1516 GSH2FL). Using the sintering parameters developed in (You, Choi, Yoon, & Lee, 2012) for iron-based MIM parts, the parts were heated up to 1250°C for 90 min under a pure hydrogen gas flow of about 30 l/min (Figure 4-3c). The sintered density was measured using the oil impregnation method based on Archimedes' principle according to MPIF standard 42 (MPIF Standard, 1986). Metallographic analyses were performed on cross-sections of the sintered parts, which were vacuum-impregnated by epoxy resin, cured at 60°C, mirror-polished, and observed using an optical microscope in unetched condition. As presented in Figure 4-3d, the debinding stage produced no significant shrinkage as compared to the injected part, while sintering resulted in a linear shrinkage of about 12%.

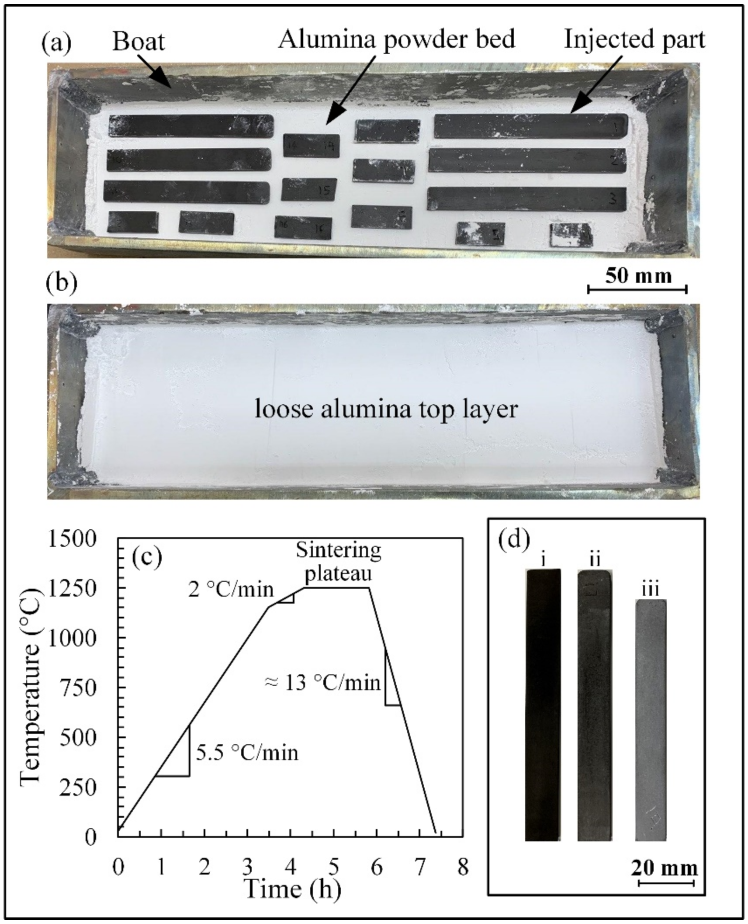
(a)
Boat
Alumina powder bed
Injected part
(b)
50 mm
loose alumina top layer
(c)
Sintering plateau
2 °C/min
≈ 13 °C/min
5.5 °C/min
Temperature (°C)
1500
1250
1000
750
500
250
0
0 1 2 3 4 5 6 7 8
Time (h)
(d)
i
ii
iii
20 mm

Figure 4-3 Debinding setup illustrating the (a) injected parts settled on a compacted alumina bed in a boat, (b) parts buried in the powder bed, (c) sintering cycle, and (d) overall dimensions of the i-injected, ii-debound, iii-sintered

4.4 Results and discussion

4.4.1 Evaluation of the maximum solid loading, melting point, and viscosity of feedstocks

It is expected that the higher the volume fraction of powder in the feedstock (also called solid loading), the smaller the shrinkage occurring during sintering. For a given feedstock, this value is set close to or slightly below the critical solid loading providing the necessary lubricity for molding. Since each powder and binder combination exhibits different powder loading capabilities, the maximum solid loadings for each feedstock were assessed from the pycnometer density profiles reported in Figure 4-4. Each feedstock density was measured three times using different samples and producing a standard deviation as low as ~0.003 g/cm^3. In this work, the critical solid loading was determined where the measured density diverged by 0.025 g/cm^3 (dashed line) from the theoretical density (continuous line). For the same powder shape, the coarser the powder, the higher the critical solid loading, which explains why the measured densities of the -45 μm, -20 μm, and -10 μm feedstocks diverged from their theoretical equivalents at ~59, 59, and 57 vol. % of powder loading, respectively. Due to its higher sphericity, the feedstock formulated with spherical CIP particles exhibited a critical solid loading of ~63 vol. %, which is significantly higher than that of the finest -10 μm irregular powder. Since preliminary injection results confirmed that the feedstocks of this study were difficult to inject due to high thickness, even into a simple shape cavity, the maximum solid loading used in this work was set at 1 vol. % below the critical solid loading, as indicated by white arrows in Figure 4-4 and reported in Table 4-3. The solid loading values presented herein were determined at room temperature, and their polymer proportion references the feedstock identification. For example, the feedstock 37PW-1SA-2CW-2EVA reported in Table 4-3 is a mixture containing 58 vol. % of powder with 37 vol. % of paraffin wax, 1 vol. % of stearic acid, 2 vol. % of carnauba wax, and 2 vol. % of ethylene-vinyl acetate.

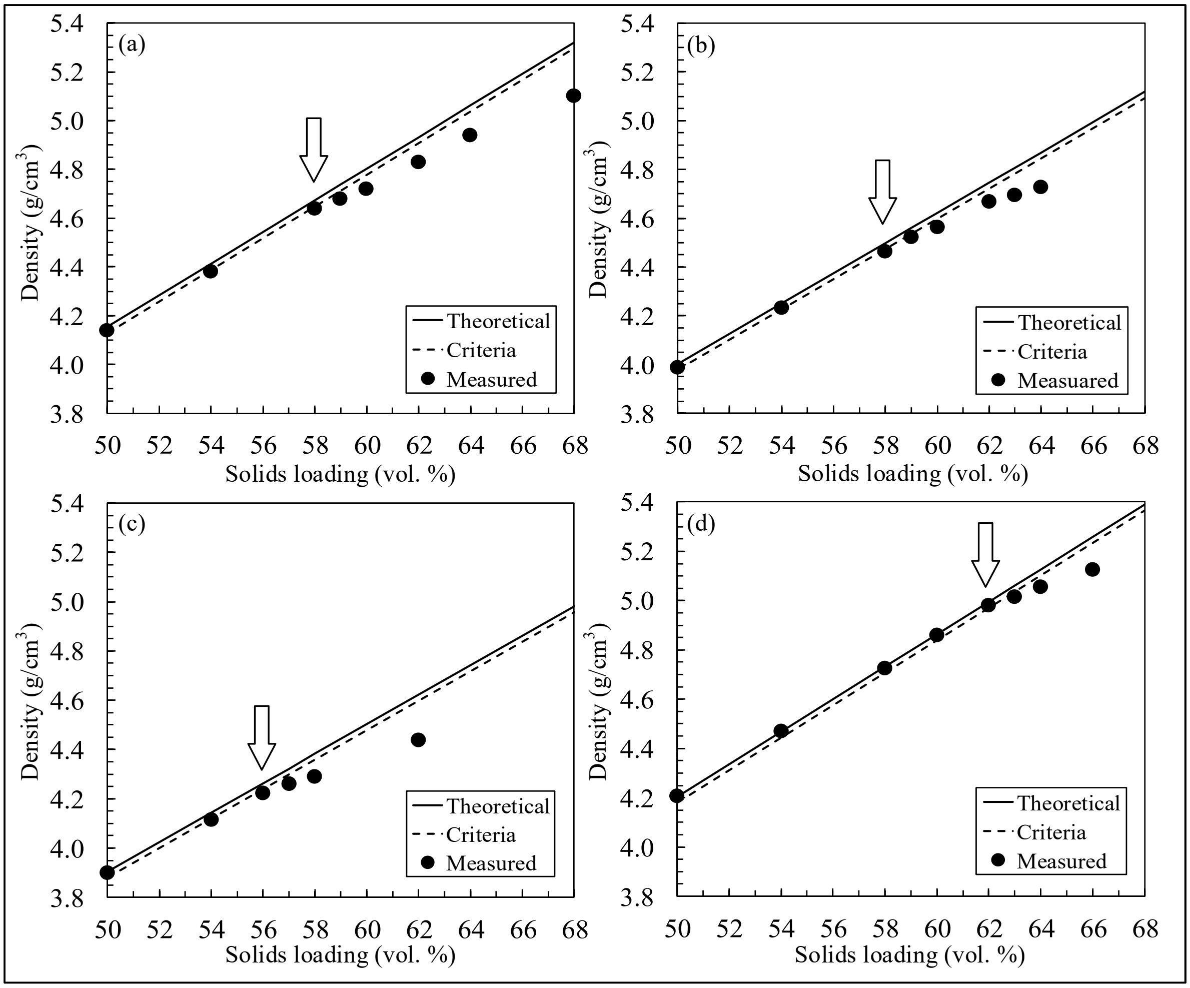

Figure 4-4 Determination of the critical and maximum solid loadings of the feedstocks prepared with (a) -45 µm, (b) -20 µm, (c) -10 µm, and (d) CIP powders

The melting points of the feedstocks were determined from the DSC peaks (2nd heating cycle), as indicated by black arrows at 58.5°C in Figure 4-5a. As expected, the powder characteristics had no impact on the feedstock melting point since this thermal property depends only on the binder formulation, which was similar for all the powder-binder mixtures. Based on this value, the temperature for the rheological tests and injection stage was set at 80°C to guarantee the molten state of the feedstocks, with adequate flowability. Other DSC peaks observed at lower temperatures, indicated by white arrows in Figure 4-5a, confirm that this multi-binder formulation exhibits several melting points. The DSC graphs also confirm that these binder constituents have a certain degree of solubility wherein the binder blend exhibits a melting point somewhere between the minimum and maximum values obtained for the single constituents (see Table 4-2).

The viscosity profiles obtained at 80°C for the four feedstocks are shown in Figure 4-5b. During injection into a simple shape cavity, our previous work (Ben Trad, Demers, Côté, Sardarian, & Dufresne, 2020) demonstrated that the typical shear rate experienced by the LPIM feedstock varies between 10 and 100 s^{-1}. In this range, a viscosity below 20 Pa·s was measured for all feedstocks, i.e., the value proposed by Hidalgo et al. (Hidalgo et al., 2012) for a typical LPIM injection. Moreover, a shear-thinning behavior was observed for all the feedstocks, with the viscosity decreasing gradually from a low to a high shear strain rate. This well-known phenomenon is attributable to the breaking up of agglomerates, particle ordering, and binder molecular chain alignment with the flow as the speed of the test increases (Foong & Tam, 1998). This rheological behavior is generally suitable for the LPIM process since having a low viscosity at higher shear rates promotes moldability during the injection stage, while having a high viscosity at low or zero shear rates minimizes segregation during the solidification stage. As expected, the lowest and the highest viscosity values were obtained with the feedstock containing the coarsest (-45 µm) and the finest (CIP) powders, respectively.

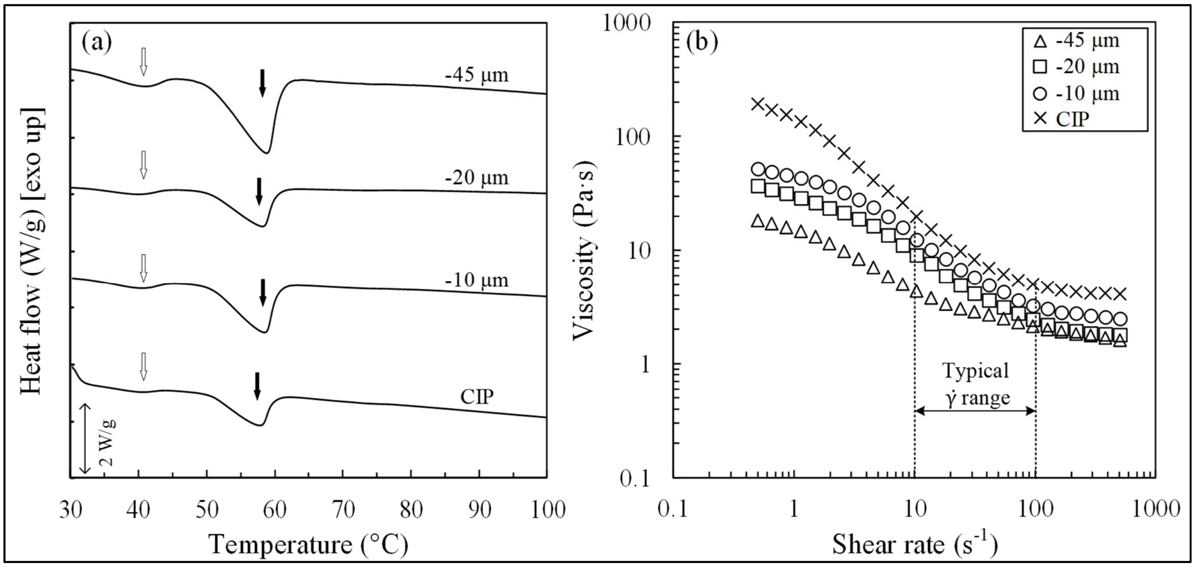

Figure 4-5 (a) DSC results obtained during heating (2nd cycle), (b) viscosity profile obtained at 80°C for feedstocks prepared with -45 µm, -20 µm, -10 µm, and CIP powders

Table 4-3 Characteristics of the feedstocks

Powder	Maximum solid loading (vol. %)	Feedstock identification
-45 µm	58	37PW-1SA-2CW-2EVA
-20 µm	58	37PW-1SA-2CW-2EVA
-10 µm	56	39PW-1SA-2CW-2EVA
CIP	62	33PW-1SA-2CW-2EVA

4.4.2 Design of the debinding cycle and characterization of the debound parts

The TGA profiles were used to determine the initial and final binder decomposition temperatures presented in Figure 4-6a. During heating, the weight loss occurring around 250°C (noted as T_{D1} in Figure 4-6a) corresponds to the beginning of the binder thermal decomposition, which mainly takes place up to 380°C (noted as T_{D2} in Figure 4-6a), and is completed at 460°C (noted as T_{D3} in Figure 4-6a). Thermal wick-debinding cycle has three sequential segments: first, to extract the molten binder from the injected part; then, to burn the binder out of the part, and finally, to pre-sinter the powder particles to ensure safe handling of the parts up to the sintering cycle. During the first segment, noted as the debinding plateau in Figure 4-6b, the temperature generally ranges from T_m to T_{D1} to guarantee a molten state of the binder, while avoiding its thermal decomposition. According to the DSC and TGA tests, the temperature for the debinding plateau was set at 250°C. Furthermore, a low heating rate of about 0.4°C/min, along with a stabilization dwell time of 2 hours, were used to produce a slow and gradual wicking process of the liquid binder (over ~12 hours) and to minimize the temperature gradients that may generate defects, cracks, or blistering inside green parts (Thomas-Vielma, Cervera, Levenfeld, & Várez, 2008). During the second segment, noted as the burnout ramp in Figure 4-6b, the liquid binder absorbed by the alumina powder bed surrounding the parts was burned out during a T_{D1} to T_{D3} temperature ramp (established from TGA results), using a heating rate as low as 0.8°C/min, to minimize the temperature gradient within the debound parts. The third segment noted as the pre-sintering plateau in Figure 4-6b, corresponds to a temperature that triggers the solid-state diffusion process and initiates particle bonds while minimizing powder surface oxidation. According to our previous study (Tafti, Demers, Majdi, Vachon, & Brailovski, 2021), the pre-sintering temperature of 650°C is required to ensure sufficient strength for the extraction of all brown parts from the wicking medium. Finally, the debinding furnace was turned off and the specimens were naturally cooled down at approximately 1.6°C/min by maintaining an argon protective atmosphere down to room temperature.

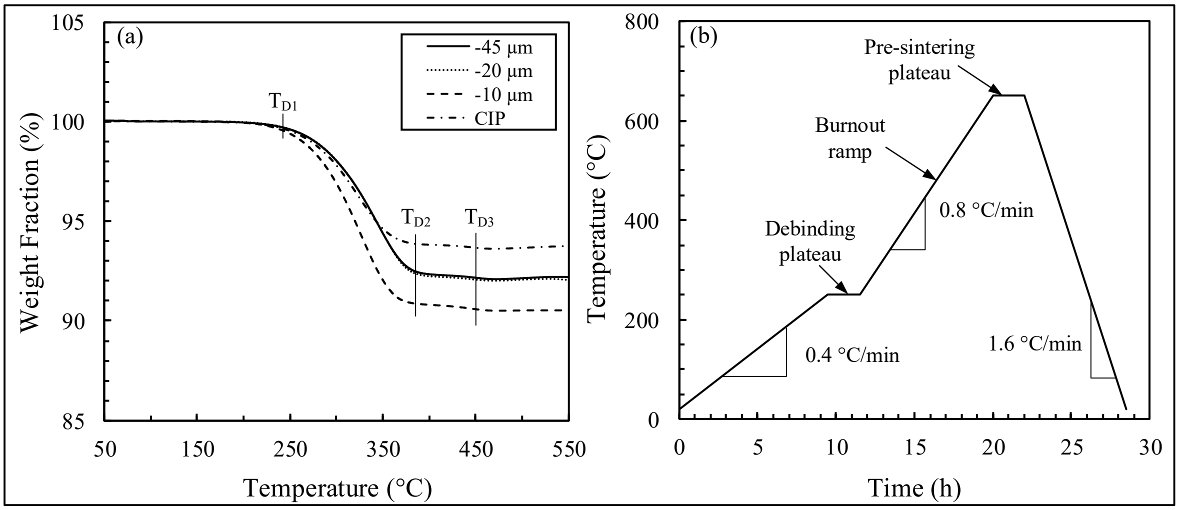

Figure 4-6 (a) TGA profiles obtained with feedstocks, (b) thermal wick-debinding profile designed based on the DSC and TGA results

The SEM observations of the debound parts presented in Figure 4-7 confirm that all the specimens had a large number of open channels (indicated by black arrows in Figure 4-7(a-d), with no visible traces of any remaining binder. However, as it is visible in Figure 4-7d, these channels were smaller in the CIP parts than in parts produced from other feedstocks. Moreover, no visible particle bonding was observed in the center of the specimens, irrespective of the powder lot. Nevertheless, as indicated by the white arrows in Figure 4-7(a-c), in specimens prepared from irregular powders, few powder clusters were observed, thus indicating the possibility of powder bonding (i.e., no clear necking at powder interfaces). Conversely, for the CIP specimens, small particles were well-distributed, and clusters were not visible (Figure 4-7d). Since brown parts mainly contain a particle network similar to that of loose powders, after this low-temperature debinding, their strength is most probably due to an occurrence of solid-state bonds at the surface of the parts and/or the powder particle interlocking.

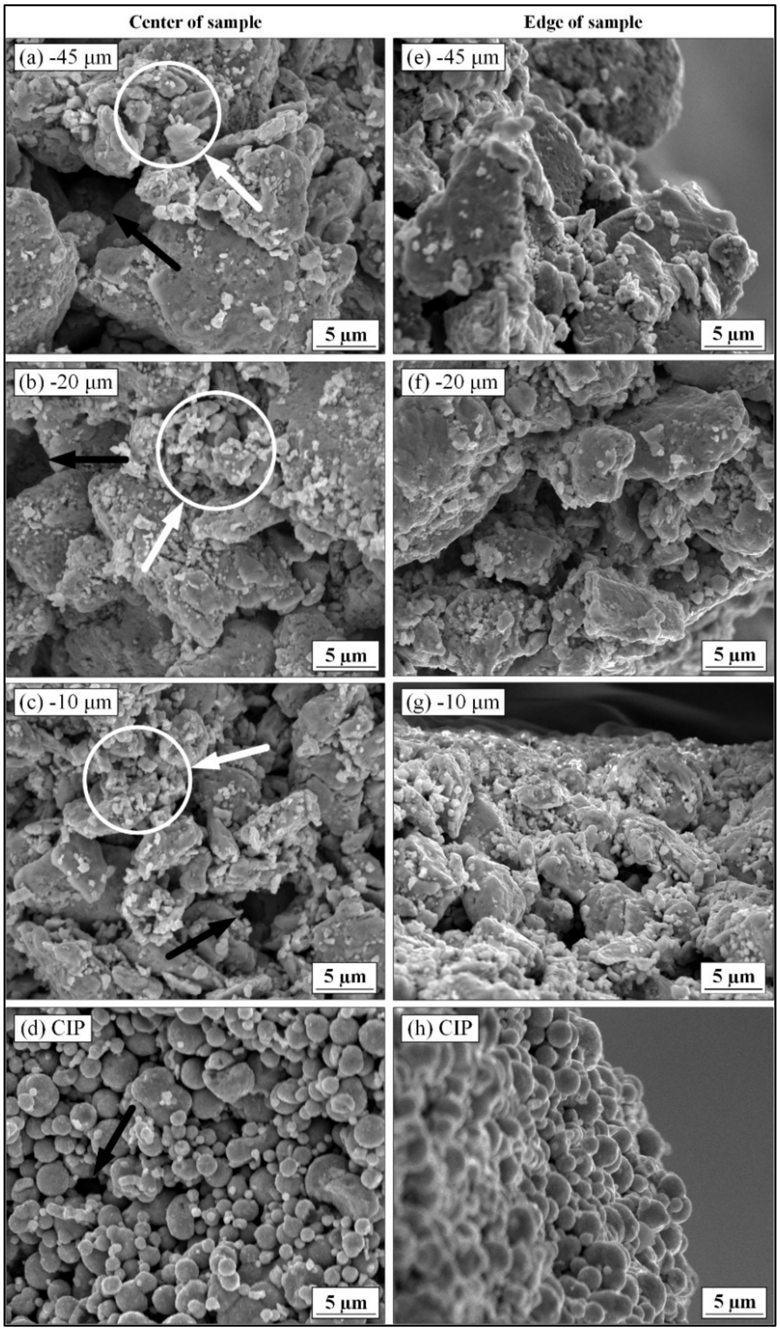
Center of sample
Edge of sample
(a) -45 μm
(b) -20 μm
(c) -10 μm
(d) CIP
(e) -45 μm
(f) -20 μm
(g) -10 μm
(h) CIP
5 μm

Figure 4-7 SEM micrographs of the cross-section (a-d) at the center (left column) and (e-h) edge (right column) of the brown specimens produced from -45 μm, -20 μm, -10 μm, and with CIP powders

4.4.3 Sintered properties

The evolution of the sintered density for the four powder conditions are presented in Figure 4-8a For irregular powders, their densities correspond to a density range varying between 6.2 and 6.6 g/cm^3, where the coarsest powder (-45 μm) exhibits the highest density value, the midrange powder (-20 μm), the lowest density value, and the finest powder (-10 μm), an intermediate density value. This unexpected trend in density values was confirmed by the metallographic observations. The metallographic observation of the -45 μm powder specimens (Figure 4-8b) exhibits a higher densification state as compared to the other irregular powders (Figure 4-8(c-d)), showing a continuous network of sintered iron (the bright phase in Figure 4-8b), along with ligamental but almost isolated pores (dark phases in Figure 4-8b). A decrease in densification capability associated with the lowest density values obtained with the -20 μm powder specimens was also confirmed by a lower amount of densified material combined with a higher number of pores and interconnectivity observed in Figure 4-8c. The degree of interconnection, as well as the number of pores seen on the metallography for the -10 μm powder specimens (Figure 4-8d), are between the other two irregular powders, reflecting its density value.

The fact that the most optimal sintered properties for these three irregular powders were obtained with the -45 μm powder specimens could be explained by a more intricate mechanism hindering the sintering, such as an increase in the oxide or soot content, as the size of irregular powder particles decreased. As expected, CIP feedstock with a higher packing density and solid loading produced the highest sintered density of 7.5 g/cm^3, which corresponds to 95% of theoretical density of iron powder. As shown in Figure 4-8e, the volume fraction of densified material is significantly higher and the proportion of pores is lower as compared to the irregular powders. However, as reported by other research groups, a higher relative density of 98% can be achieved with CIP powder using higher sintering temperatures (Shin, Jung, Kim, & Park, 2018). This sintering process would need to be further optimized for each of the powder feedstocks used in this study to confirm if higher densification is achievable.

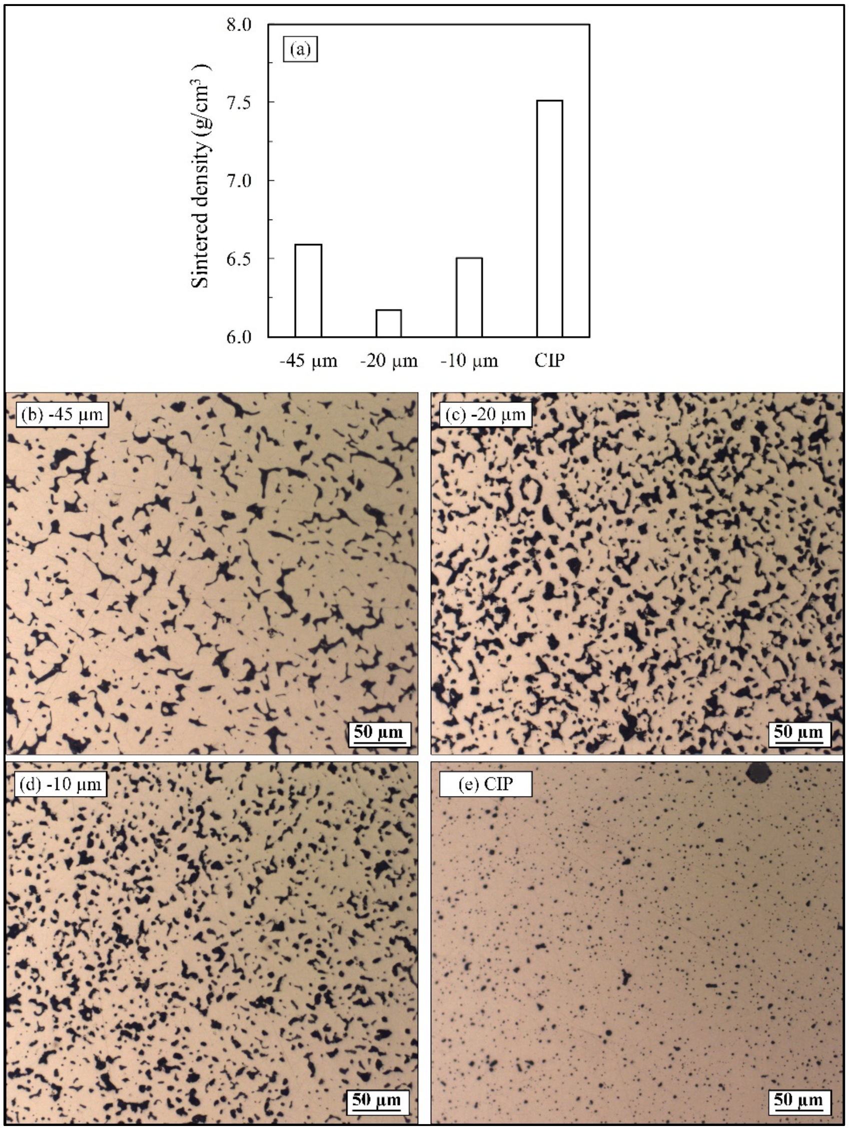

Figure 4-8 (a) Sintered density and optical micrographs of (b) -45 µm, (c) -20 µm, (d) -10 µm, (e) CIP as-polished specimens after sintering (bright phase: iron, and black phase: pores)

4.5 Conclusion

Iron parts were produced via the low-pressure powder injection molding (LPIM) technique using irregular and spherical iron-based feedstocks. Four low-viscosity feedstocks were formulated from three different irregular ($5.0 < D_{50} < 18.3$ µm) powders and one spherical ($D_{50} = 4$ µm) iron-based powder using a common binder system containing paraffin wax, carnauba wax, stearic acid, and ethylene-vinyl acetate. The four feedstocks were injected into a rectangular mold cavity, thermally wick-debound (debinding plateau at 250°C and pre-sintering plateau at 650°C under argon atmosphere for 30 h) and sintered (1250°C under a hydrogen atmosphere for 90 min). The conclusions are summarized as follows:

- The low-viscosity and low melting point (η < 20 Pa·s; $T_m \approx 59$°C) of feedstocks confirm that the irregular iron powders sieved at -45, -20, and -10 µm, as well as the spherical iron powder with a D_{50} as low as 4 µm, can be shaped via the LPIM process.
- The maximum solid loadings obtained with irregular (56-58 vol. %) and spherical (62 vol. %) powders represent the expected values for these two powder morphologies.
- CIP powder exhibits the highest sintered density of ~7.5 g/cm^3. Among the irregular powders, the -45 µm powder produces the highest sintered density at ~6.6 g/cm^3. The metallographic observations confirm these density values.
- To the best of the authors' knowledge, the low-pressure powder injection molding has been used, for the first time in this study, to produce iron parts from irregular iron powders in which results in producing the MIM parts with a lower cost eventually.

4.6 Acknowledgments

This work was carried out with the financial support of the Natural Sciences and Engineering Research Council of Canada (Grant CRDPJ505289-16). The authors wish to thank Mr. Raphael Cote and Mr. Francis Ares for their collaboration in TGA and injection tests.

CONCLUSIONS

The objective of this Master's research was to investigate the effects of particle size and shape on the injection, debinding, and sintering properties of iron-based feedstocks for low-pressure injection molding in an experimental setting. Up to this point, efforts to improve the moldability of iron-based powders have yielded positive results. Still, the properties of LPIM parts prepared from iron-based powders, which typically involve debinding and sintering, have not been characterized. To support a better understanding of the fundamental mechanisms underlying the debindability and sinterability of iron-based LPIM feedstocks, this work studies the impact of the particle shape and size on the debinding and sintering properties of parts molded with these feedstocks.

In this work, the initial feedstocks were formulated according to our previous study, which exhibits the optimization for further experiments. Pycnometer-measured density was used to formulate and determine the feedstock critical solid loading. To facilitate the demolding operation, the maximum solid loading of powders was set at 1 vol. % lower than the critical solid loading. The feedstock melting point was obtained from the DSC micrograph and used to define the temperatures of the rheological tests and the injection. The viscosity of all feedstocks decreases as the shear rate increases showing the shear thinning behavior generally required for the LPIM feedstocks. The debinding cycle was designed according to the data obtained using the TGA tests. Our initial debinding tests revealed that pre-sintering temperatures lower than 650 °C results in insufficient bonding, while pre-sintering temperatures higher than 650 °C increase the potential oxidation and layering of debound samples. The CIP powder exhibited the highest density among all the given powders, while the -45 μm powder produced the highest density among the irregular powders of this study. The metallographic observations were in line with the density values. The results obtained reveal the interrelations between the particle shape and size and the debinding and sintering characteristics of parts molded with iron-based feedstock using the LPIM process.

RECOMMENDATIONS

Following the previously mentioned conclusions, some recommendations can be drawn for future works in the LPIM research group at ÉTS, which are:

- Based on the new developments made during this research, it is suggested that defections that occur during the injection process be minimized to obtain injected parts with the lowest deflection (e.g., void-free part after injection), which is critical for achieving better debound and sintered physical and micro-structural properties of sintered parts.
- Optimizing the debinding and sintering heating cycles depending on each powder's characteristics can contribute to reduce possible oxidation and improve physical and micro-structural properties of final components.
- Mechanical properties testing to observe the influence of particle shape and size on their mechanical performance of fully sintered parts.

REFERENCES

Adames, J. M. (2007). *Characterization of polymeric binders for metal injection molding (MIM) process*. University of Akron.

Ali, M., & Ahmad, F. (2020). Influence of powder loading on rheology and injection molding of Fe-50Ni feedstocks. *Materials and Manufacturing Processes*, *00*(00), 1–11. https://doi.org/10.1080/10426914.2020.1734616

Amin, S. Y. M., Jamaludin, K. R., & Muhamad, N. (2009). Rheological Properties of Ss316L Mim Feedstock Prepared With Different Particle Sizes and Powder Loadings. *The Institution of Engineers, Malaysia*, *71*(2), 59–63.

ASTM International. (2015). *D3418-15 Standard Test Method for Transition Temperatures and Enthalpies of Fusion and Crystallization of Polymers by Differential Scanning Calorimetry*. *ASTM Standard*. Conshohocken, PA: ASTM International. https://doi.org/https://doi.org/10.1520/D3418-15

ASTM International. (2016). Standard Test Method for Metal Powder Skeletal Density by Helium or Nitrogen. *ASTM International*. West Conshohocken, PA: ASTM International. https://doi.org/https://doi.org/10.1520/B0923-20

Atre, S. V, Weaver, T. J., & German, R. M. (1998). *Injection molding of metals and ceramics*. SAE Technical Paper.

Ben Trad, M. A., Demers, V., Côté, R., Sardarian, M., & Dufresne, L. (2020). Numerical simulation and experimental investigation of mold filling and segregation in low-pressure powder injection molding of metallic feedstock. *Advanced Powder Technology*, *31*(3), 1349–1358. https://doi.org/10.1016/j.apt.2020.01.018

Binet, C., Heaney, D. F., Spina, R., & Tricarico, L. (2005). Experimental and numerical analysis of metal injection molded products. *Journal of Materials Processing Technology*, *164–165*, 1160–1166. https://doi.org/10.1016/j.jmatprotec.2005.02.128

Contreras, J. M., Jiménez-Morales, A., & Torralba, J. M. (2009). Fabrication of bronze components by metal injection moulding using powders with different particle characteristics. *Journal of Materials Processing Technology*, *209*(15–16), 5618–5625. https://doi.org/10.1016/j.jmatprotec.2009.05.021

Dehghan-Manshadi, A., Yu, P., Dargusch, M., StJohn, D., & Qian, M. (2020). Metal injection moulding of surgical tools, biomaterials and medical devices: A review. *Powder Technology*, *364*, 189–204. https://doi.org/10.1016/j.powtec.2020.01.073

Demers, V., Turenne, S., & Scalzo, O. (2015). Impact of binders on viscosity of low-pressure powder injection molded Inconel 718 superalloy. *Journal of Materials Science*, *50*(7), 2893–2902. https://doi.org/10.1007/s10853-015-8853-z

Demers, Vincent. (2019). Journal of Insurance Medicine. *Journal of Insurance Medicine*, *45*(1), 1–2. https://doi.org/10.17849/0743-6661-45.1.1

Dimitri, C., Mohamed, S., Thierry, B., & Jean-Claude, G. (2017). Influence of particle-size distribution and temperature on the rheological properties of highly concentrated Inconel feedstock alloy 718. *Powder Technology*, *322*, 273–289. https://doi.org/10.1016/j.powtec.2017.08.049

Fareh, F., Demers, V., Demarquette, N. R., Turenne, S., & Scalzo, O. (2017). Influence of segregation on rheological properties of wax-based feedstocks. *Powder Technology*, *320*, 273–284. https://doi.org/10.1016/j.powtec.2017.07.056

Foong, M. L., & Tam, K. C. (1998). Application of Polymer Technology to Metal Injection Molding (MIM) Processing. In *Advanced polymer processing operations* (pp. 213–280). Elsevier.

German, R. M. (2012). Metal powder injection molding (MIM): Key trends and markets. *Handbook of Metal Injection Molding*, (Mim), 1–25. https://doi.org/10.1533/9780857096234.1

German, R M. (1990). Powder injection molding, MPIF. *Princeton, New Jersey*.

German, Randall M., Hens, K. F., & Kin, S.-T. P. (1991). Key Issues in Powder Injection-Molding. *Ceramic, American Bulletin, Society*, *70*(8), 1294–1302.

German, Randall M, & Bose, A. (1997). *Injection molding of metals and ceramics. Metal Powder Industries Federation, Princeton, NJ.*

Gonçalves, A. C. (2001). Metallic powder injection molding using low pressure. *Journal of Materials Processing Technology*, *118*(1–3), 193–198. https://doi.org/10.1016/S0924-0136(01)00916-5

Gonçalves, Aparecido Carlos. (2001). Metallic powder injection molding using low pressure. *Journal of Materials Processing Technology*, *118*(1–3), 193–198. https://doi.org/10.1016/S0924-0136(01)00916-5

González-gutiérrez, J., Stringari, G. B., & Emri, I. (2012). Powder Injection Molding of Metal and Ceramic Parts, Some Critical Issues for Injection Molding. *Some Critical Issues for Injection Molding*, 65–88. https://doi.org/10.1126/science.1094581

Gorjan, L. (2012). Wick Debinding - An Effective Way of Solving Problems in the Debinding Process of Powder Injection Molding. *Some Critical Issues for Injection Molding*. https://doi.org/10.5772/34969

Gorjan, L., Dakskobler, A., & kosmač, T. (2010). Partial wick-debinding of low-pressure powder injection-moulded ceramic parts. *Journal of the European Ceramic Society*, *30*(15), 3013–3021. https://doi.org/10.1016/j.jeurceramsoc.2010.07.011

Hashikawa, R., Osada, T., Kudo, K., Tsumori, F., & Miura, H. (2016). Control the distortion of the large and complex shaped parts by the metal injection molding process. *Funtai Oyobi Fummatsu Yakin/Journal of the Japan Society of Powder and Powder Metallurgy*, *63*(7), 473–478. https://doi.org/10.2497/jjspm.63.473

Hausnerova, B. (2011). Powder injection moulding-An alternative processing method for automotive items. *New Trends and Developments in Automotive System Engineering*, 129–145.

Hausnerova, B., Mukund, B. N., & Sanetrnik, D. (2017). Rheological properties of gas and water atomized 17-4PH stainless steel MIM feedstocks: Effect of powder shape and size. *Powder Technology*, *312*, 152–158. https://doi.org/10.1016/j.powtec.2017.02.023

Hausnerová, B., Sáha, P., & Kubát, J. (1999). Capillary Flow of Hard-Metal Carbide Powder Compounds. *International Polymer Processing*, *14*(3), 254–260. https://doi.org/10.3139/217.1556

Hayat, M. D., Goswami, A., Matthews, S., Li, T., Yuan, X., & Cao, P. (2017). Modification of PEG/PMMA binder by PVP for titanium metal injection moulding. *Powder Technology*, *315*, 243–249. https://doi.org/10.1016/j.powtec.2017.04.004

Heaney, D.F. (2019). *Qualification of metal injection molding (MIM)*. *Handbook of Metal Injection Molding* (2nd ed.). Elsevier Ltd. https://doi.org/10.1016/b978-0-08-102152-1.00015-5

Heaney, Donald F. (2012). *Handbook of metal injection molding*. Elsevier.

Heaney, Donald F. (2018). *Handbook of metal injection molding*. Woodhead Publishing.

Herranz, G. (2019). *Control of carbon content in metal injection molding*. *Handbook of Metal Injection Molding* (2nd ed.). Elsevier Ltd. https://doi.org/10.1016/b978-0-08-102152-1.00016-7

Hidalgo, J., Jiménez-Morales, A., & Torralba, J. M. (2012). Torque rheology of zircon feedstocks for powder injection moulding. *Journal of the European Ceramic Society*, *32*(16), 4063–4072. https://doi.org/10.1016/j.jeurceramsoc.2012.06.023

Ho, Y. L., & Lin, S. T. (1995). Debinding variables affecting the residual carbon content of injection-molded Fe-2 Pct Ni steels. *Metallurgical and Materials Transactions A*, *26*(1), 133–142. https://doi.org/10.1007/BF02669799

Hu, Y., Li, Y., Lou, J., He, H., Li, L., Li2, Y., … Li, L. (2018). Potential of Manufacturing Low Cost MIM Stainless Steel. *Int J Metall Met Phys*, *3*, 17.

Hwang, K. S., Lin, H. K., & Lee, S. C. (1997). Thermal, solvent, and vacuum debinding mechanisms of PIM compacts. *Materials and Manufacturing Processes*, *12*(4), 593–608. https://doi.org/10.1080/10426919708935169

Kankawa, Y. (1997). Effects of polymer decomposition behavior on thermal debinding process in metal injection molding. *Materials and Manufacturing Processes*, *12*(4), 681–690. https://doi.org/10.1080/10426919708935175

Kong, X., Barriere, T., & Gelin, J. C. (2012). Determination of critical and optimal powder loadings for 316L fine stainless steel feedstocks for micro-powder injection molding. *Journal of Materials Processing Technology*, *212*(11), 2173–2182. https://doi.org/10.1016/j.jmatprotec.2012.05.023

Koseski, R. P., Suri, P., Earhardt, N. B., German, R. M., & Kwon, Y. S. (2005). Microstructural evolution of injection molded gas- and water-atomized 316L stainless steel powder during sintering. *Materials Science and Engineering A*, *390*(1–2), 171–177. https://doi.org/10.1016/j.msea.2004.08.002

Kryachek, V. M. (2004). Injection moulding. *Powder Metallurgy and Metal Ceramics*, *43*(7–8), 336–348.

Lamarre, S. G., Demers, V., & Chatelain, J. F. (2017). Low-pressure powder injection molding using an innovative injection press concept. *International Journal of Advanced Manufacturing Technology*, *91*(5–8), 2595–2605. https://doi.org/10.1007/s00170-016-9889-1

Liberati, J. F., Araujo Filho, O. O., Monteiro, W. A., Esposito, I. M., Nogueira, R. A., & Ambrosio Filho, F. (2006). Low-pressure injection molding processing of AISI T15 high speed steel powders. *Materials Science Forum*, *514–516*(PART 1), 569–573. https://doi.org/10.4028/www.scientific.net/MSF.514-516.569

Mamen, B., Song, J., Barriere, T., & Gelin, J. C. (2015). Experimental and numerical analysis of the particle size effect on the densification behaviour of metal injection moulded tungsten parts during sintering. *Powder Technology*, *270*(Part A), 230–243. https://doi.org/10.1016/j.powtec.2014.10.019

Mangels, J. A. (1994). Low-pressure injection molding. *American Ceramic Society Bulletin;(United States)*, *73*(5).

Medvedovski, E., & Peltsman, M. (2012). Low pressure injection moulding mass production technology of complex shape advanced ceramic components. *Advances in Applied Ceramics*, *111*(5–6), 333–344. https://doi.org/10.1179/1743676112y.0000000025

MPIF Standard. (1986). Determination of Density of Compacted or Sintered Metal Powders, 42. *Princeton, NJ*, 2–6.

Mukund, B. N., & Hausnerova, B. (2020). Variation in particle size fraction to optimize metal injection molding of water atomized 17–4PH stainless steel feedstocks. *Powder Technology*, *368*, 130–136. https://doi.org/10.1016/j.powtec.2020.04.058

Park, S. J., Wu, Y., Heaney, D. F., Zou, X., Gai, G., & German, R. M. (2009). Rheological and thermal debinding behaviors in titanium powder injection molding. *Metallurgical and Materials Transactions A: Physical Metallurgy and Materials Science*, *40*(1), 215–222. https://doi.org/10.1007/s11661-008-9690-3

Piotter, V., Bauer, W., Knitter, R., Mueller, M., Mueller, T., & Plewa, K. (2011). Powder injection moulding of metallic and ceramic micro parts. *Microsystem Technologies*, *17*(2), 251–263. https://doi.org/10.1007/s00542-011-1274-2

Quevedo Nogueira, R. E. F., Bezerra, A. C., dos Santos, F. C., Sousa, M. R. de, & Acchar, W. (2001). Low-Pressure Injection Molding of Alumina Ceramics Using a Carnauba Wax Binder: Preliminary Results. *Key Engineering Materials*, *189–191*, 67–72. https://doi.org/10.4028/www.scientific.net/KEM.189-191.67

Rane, K., & Date, P. (2019). Evolution of properties of parts during MIM and sintering of recycled oxide particles. *Powder Metallurgy*, *62*(2), 133–145. https://doi.org/10.1080/00325899.2019.1603621

Rane, K. K., & Date, P. P. (2014). Rheological Investigation of MIM Feedstocks for Reducing Frictional Effects during Injection Moulding. In *Advanced Materials Research* (Vol. 966–967, pp. 196–205). https://doi.org/10.4028/www.scientific.net/amr.966-967.196

Rei, M., Milke, E. C., Gomes, R. M., Schaeffer, L., & Souza, J. P. (2002). Low-pressure injection molding processing of a 316-L stainless steel feedstock. *Materials Letters*, *52*(4–5), 360–365. https://doi.org/10.1016/S0167-577X(01)00422-0

Ruprecht, R., Gietzelt, T., Müller, K., Piotter, V., & Haußelt, J. (2002). Injection molding of microstructured components from plastics, metals and ceramics. *Microsystem Technologies*, *8*(4–5), 351–358.

Santos, M. A. dos, Neivock, M. P., Maliska, A. M., Klein, A. N., & Muzart, J. L. R. (2005). Plasma debinding and pre-sintering of injected parts. *Materials Research*, *7*(3), 505–511. https://doi.org/10.1590/s1516-14392004000300021

Schlechtriemen, N., Knitter, R., Haußelt, J., & Binder, J. R. (2013). Impact of powder morphology on quality of low-pressure injection moulded reaction-bonded net shape oxide ceramics. *Journal of the European Ceramic Society*, *33*(4), 709–715. https://doi.org/10.1016/j.jeurceramsoc.2012.10.010

Shin, D. S., Jung, I. D., Kim, H. J., & Park, S. J. (2018). Development of powder injection molding process for sintered soft magnet with the addition of Fe-17 at.% P powder. *Metal Powder Report*, *73*(1), 38–45. https://doi.org/10.1016/j.mprp.2017.06.029

Shu, G. J., & Hwang, K. S. (2004). High density powder injection molded compacts prepared from a feedstock containing coarse powders. *Materials Transactions*, *45*(10), 2999–3004. https://doi.org/10.2320/matertrans.45.2999

Sotomayor, M. E., Várez, A., & Levenfeld, B. (2010). Influence of powder particle size distribution on rheological properties of 316L powder injection moulding feedstocks. *Powder Technology*, *200*(1–2), 30–36. https://doi.org/10.1016/j.powtec.2010.02.003

Tafti, A. A., Demers, V., Majdi, S. M., Vachon, G., & Brailovski, V. (2021). Effect of Thermal Debinding Conditions on the Sintered Density of Low-Pressure Powder Injection Molded Iron Parts. *Metals* . https://doi.org/10.3390/met11020264

Tafti, A. A., Demers, V., Vachon, G., & Brailovski, V. (2021). Effect of Binder Constituents and Solids Loading on the Rheological Behavior of Irregular Iron-Based Feedstocks. *Journal of Manufacturing Science and Engineering, Transactions of the ASME*, *143*(3), 1–12. https://doi.org/10.1115/1.4048268

Thomas-Vielma, P., Cervera, A., Levenfeld, B., & Várez, A. (2008). Production of alumina parts by powder injection molding with a binder system based on high density polyethylene. *Journal of the European Ceramic Society*, *28*(4), 763–771. https://doi.org/10.1016/j.jeurceramsoc.2007.08.004

Vervoort, P. J., Vetter, R., & Duszczyk, J. (1996). Overview of powder injection molding. *Advanced Performance Materials*, *3*(2), 121–151. https://doi.org/10.1007/BF00136742

Wikimedia Foundation, I. (2021). INDO-MIM_Automotive_Sector_. Retrieved from https://en.wikipedia.org/wiki/Metal_injection_molding

Wongpanit, P., Khanthsri, S., Puengboonsri, S., & Manonukul, A. (2014). Effects of acrylic acid-grafted HDPE in HDPE-based binder on properties after injection and debinding in metal injection molding. *Materials Chemistry and Physics*, *147*(1–2), 238–246. https://doi.org/10.1016/j.matchemphys.2014.04.035

Ye, Y., Qiao, L., Zheng, J., Ying, Y., Li, W., Yu, J., … Jiang, L. (2017). Effect of microcrystalline wax on the solvent debinding of the Sr-ferrite ceramics prepared by powder injection molding. *Journal of the European Ceramic Society*, *37*(5), 2105–2114. https://doi.org/10.1016/j.jeurceramsoc.2016.12.026

You, W. K., Choi, J. P., Yoon, S. M., & Lee, J. S. (2012). Low temperature powder injection molding of iron micro-nano powder mixture. *Powder Technology*, *228*, 199–205. https://doi.org/10.1016/j.powtec.2012.05.016

Zorzi, J. E., Perottoni, C. A., & Da Jornada, J. A. H. (2002). Hard-skin development during binder removal from Al2O3-based green ceramic bodies. *Journal of Materials Science*, *37*(9), 1801–1807. https://doi.org/10.1023/A:1014949923939